

Measurement of single top quark production in association with W, Z, or Higgs boson in ATLAS

Kanhaiya Gupta

Masterarbeit in Physik
angefertigt im Physikalischen Institut

vorgelegt der
Mathematisch-Naturwissenschaftlichen Fakultät
der
Rheinischen Friedrich-Wilhelms-Universität
Bonn

January 2022

I hereby declare that this thesis was formulated by myself and that no sources or tools other than those cited were used.

Bonn,
Date
Signature

1. Gutachter: Prof. Dr. Ian C. Brock
2. Gutachterin: Prof. Dr. Klaus Desch

For my friends and supporters

Contents

1	Introduction	1
2	Theoretical concepts	3
2.1	The standard model of particle physics	3
2.1.1	Fermions	3
2.1.2	Bosons	4
2.2	Physics at hadron colliders	4
2.3	Top quark physics	4
2.3.1	Top quark	5
2.3.2	Top quark production	5
3	The LHC and the ATLAS experiment	9
3.1	The LHC	9
3.2	The ATLAS detector	10
3.2.1	The ATLAS coordinate system	11
3.2.2	Inner detector	12
3.2.3	Calorimetry	12
3.2.4	Muon system	13
3.2.5	Trigger system	13
3.3	Physics objects reconstruction in ATLAS	14
3.3.1	Electrons	14
3.3.2	Muons	14
3.3.3	Jets	14
3.3.4	B-jets	14
3.3.5	Missing transverse energy	15
4	Data and Monte Carlo simulated events	17
4.1	Data sample	17
4.2	Monte Carlo simulation	18
4.2.1	Signal sample	18
4.2.2	Background sample	18
4.2.3	Reweighting of Monte-Carlo simulated events	19
4.2.4	Luminosity reweighting	19

5 Events selection	21
5.1 Signal region	21
5.1.1 Full event reconstruction	22
5.1.2 Lepton isolation working point	23
5.1.3 Optimization of cuts	25
5.1.4 Signal regions (SRs) plots and yields	27
5.2 Control regions (CRs)	29
5.2.1 Diboson CRs plots and yields	29
5.2.2 $t\bar{t}Z$ CRs plots and yield	31
5.2.3 $t\bar{t}$ CRs plots and yields	32
6 Analysis	35
6.1 Cross-section measurement analysis strategy	35
6.2 Signal and background separation	35
6.3 Multivariate analysis technique: Artificial Neural Network (NN)	36
6.3.1 Input variables	37
6.3.2 Data and MC comparison	37
6.3.3 NN training in the SRs and $t\bar{t}Z$ CRs	41
6.4 Signal extraction - Binned likelihood fit	42
6.4.1 Fitted regions	46
6.4.2 Binning optimization	46
6.5 Systematics uncertainties	47
6.5.1 Sources of systematics uncertainties	47
6.5.2 Experimental uncertainties	47
6.5.3 Theoretical uncertainties	48
6.5.4 Symmetrizing, smoothing and pruning	48
7 Results	49
7.1 Expected fit results	49
7.2 Observed fit results	51
7.3 Discussion of the results	57
8 Conclusion	59
Bibliography	61

CHAPTER 1

Introduction

The top quark is the most massive particle in the standard model (SM) of particle physics, which arise predominantly from the production of top quark-antiquark ($t\bar{t}$) pairs through the strong interaction. However top quarks may also be produced singly from electroweak processes: t-channel, s-channel and associated tW production. The D0 and CDF collaborations [1, 2] as well as the ATLAS [3] and CMS [4] collaborations have measured the cross-sections for single top quark production. The high integrated luminosity and the center-of-mass energy at the LHC allows the study of processes with very small cross-sections that were not accessible at lower energies such as the production of a single top quark in association with a Z boson. In this production mechanism the top quark is produced via the t-channel and the Z boson is either radiated off from one of the participating quarks or produced via W boson fusion leading to a signature with a single top quark, a Z boson and an additional quark. The process is sensitive to top quark couplings to the Z boson and also to the triple gauge-boson coupling (WWZ). The measurement of tZq production are also sensitive to processes beyond the SM.

In this thesis, the tZq cross-section measurement are performed in the trilepton final states, where both the W boson from the top quark and the Z boson decay into either electrons or muons, resulting in four possible leptonic combinations in the final state: eee , $ee\mu$, $e\mu\mu$, $\mu\mu\mu$ and there is also a contributions from leptonic τ decays. The thesis is structured as follows: Chapter 2 presents an overview of the SM of particle physics. It also explains the concepts related to physics at hadron colliders that are needed in order to understand the analysis. The last section presents the detail on top quark physics including the rare single top production processes. It also describes how fundamental physics objects are reconstructed from the detector information. The data and the Monte Carlo simulated samples that are used for modelling the signal and background processes are described in chapter 4. Chapter 5 begins the description of the final state of the tZq process. Several signal regions and control regions are also defined to constrain the backgrounds, each containing different contributions from signal and background processes. It also presents analysis of the lepton working point and optimization of selection cuts. In chapter 6, the measurements are performed based on multivariate analysis where artificial neural networks (NN) training are used to enhance the signal-to-background separation. The sources of systematic uncertainties that need to be taken into account for the final cross-section measurement are also presented. A binned likelihood fit is performed to extract the signal strength, which is explained in the last section. A discussion of the fit results obtained using both an asimov dataset and the real data is included in chapter 7. The thesis is concluded in chapter 8.

CHAPTER 2

Theoretical concepts

This chapter provides a brief introduction of the standard model of particle physics as well as the key concepts related to physics at hadron colliders. A brief introduction of top quark physics which is crucial for analysis in this thesis, is also presented in this chapter.

2.1 The standard model of particle physics

The standard model of particle physics (SM) is the theory describing three of the four known fundamental forces in the universe, as well as classifying all known elementary particles. The fundamental forces explained by SM are electromagnetic, weak and strong interactions, while omitting gravity. The SM is a gauge theory of quantum fields, a mathematical framework combining classical field theory, special relativity and quantum mechanics. It utilizes a Lagrangian in order to describe the dynamics of the quantum state and fundamental fields. This Lagrangian is invariant under $SU(3)_C \times SU(2)_L \times U(1)_Y$ symmetry group [5]. The strong interaction is represented by the $SU(3)_C$ group, while the unified electroweak interaction is represented by the $SU(2)_L \times U(1)_Y$ group.

Each force operates on a different on a different range and with different strengths. The strong and weak forces are very limited range and dominate only on the level of subatomic interactions, while electromagnetic forces have infinite range. The SM consists of 17 fundamental particles classified into two groups: half-integer spin fermions, and integer spin bosons. The spin-1 (vector) bosons act as the mediators of interaction between particles and the spin-0 (scalar) Higgs boson acts as the mediator of Higgs interactions. An illustration of SM particles with their mass, charge and spin is presented in figure 2.1.

2.1.1 Fermions

There are 12 spin- $\frac{1}{2}$ fermions in the SM: 6 quarks and 6 leptons, which are grouped into 3 generations which are grouped into 3 generations. Each generation of quark contains one quark of charge $+2/3e$ (up-type) and one quark of charge $-1/3e$ (down-type). The quarks are (up-type followed by down-type): up (u) and down (d); charm (c) and strange (s); and top (t) and bottom (b). Similarly three lepton generations consists of electron (e), muon (μ), and tau (τ), and their corresponding neutrinos (ν_e , ν_μ , ν_τ). The neutrinos have no electric charge, while the other leptons carry an electric charge of $-1e$.

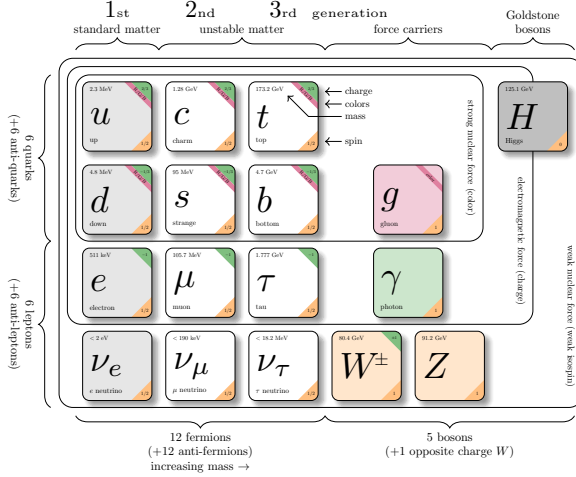


Figure 2.1: Standard Model of Particle Physics [6]

Each fermion has its corresponding anti-particle, with opposite sign on all charges (such as electric charge & quantum numbers) but identical mass.

In the SM, a quark of one flavor can transform into a quark of another flavor via weak interaction. It strongly prefer to transform into another quark of its same generation. The transformation probability scale with the couplings in the Cabibbo-Kobayashi-Masakawa (CKM) matrix. For more details. Ref. [7] can be referred.

2.1.2 Bosons

The remaining five particles in the SM are comprised of four vector type (spin-1) boson and one scalar type (spin-0) Higgs boson. Apart from the Higgs boson, all other bosons are called gauge bosons and are the mediators of the fundamental interactions between particles. Photons are the mediators of the electromagnetic force and are massless. The massive W and Z bosons ($m_W = 80.379$ GeV, $m_Z = 91.1876$ GeV) are the mediators of the weak force while strong force is mediated by massless gluons. The gluons as well as quarks carry colour charge. There are three different colour charges: red, green, and blue. Additionally, there are also three anticolours (for antiparticles). Gluons themselves carry a combination of a colour and an anticolour charge and therefore they can couple to each other. There are only eight gluons in total because one of the nine colour combinations results in a non-existing colour singlet state.

2.2 Physics at hadron colliders

2.3 Top quark physics

The neutral Kaon decays experiment in 1964 by Christenson, Cronin, Fitch, and Turlay showed that weak interaction is not invariant under the combined discrete symmetry operation of charge

conjugation C and parity P (CP violation) [8]. Kobayashi and Maskawa realized that SM can provide a mechanism of CP violation through flavor mixing only if there are at least three generations of quarks [9]. After the discovery of bottom quark in 1977 in Fermilab [10], the existence of the top quark as the weak isospin was expected. The top quark was first observed by the D0 and CDF collaborations on the Tevatron in $p\bar{p}$ collisions in 1995 [11, 12]. Nowadays LHC is a top quark factory where top quarks are produced as discussed in section 2.3.2 .

at

2.3.1 Top quark

The top quark is the heaviest fundamental particle in the SM. It is up-type third generation quark. It has an electric charge $Q = \frac{2}{3}$, a mass of $173.3 \text{ GeV}/c^2$ and a decay width of $\Gamma_t(\alpha_s(M_Z) = 0.118) = 1.35 \text{ GeV}/c^2$ which corresponds to an average lifetime of $\tau_t \approx 0.5 \times 10^{-24} \text{ s}$ [13]. The top quark exclusively decays via weak interaction before hadronization, producing a W boson and a bottom quark because of its extremely short-lived lifetime. The absence of a hadron surrounding the top quark produces physicists with the unique opportunity to study the behaviour of a "bare" quark.

2.3.2 Top quark production

Top quarks are dominantly produced in pairs through quark anti-quark annihilation and gluon-gluon fusion at leading order in QCD at hadron colliders such as Tevatron and LHC. They are also produced singly through electroweak processes. At the LHC, top-quarks are mainly produced via gluon-gluon fusion. In this production mechanism two gluons from protons fuse into another gluon (see figure 2.2(a) and 2.2(b)) , or they exchange a virtual top quark and then emit a real $t\bar{t}$ pair (see figure 2.2(c)). Figure 2.2 shows the leading order Feynman diagrams producing top anti-top pairs.

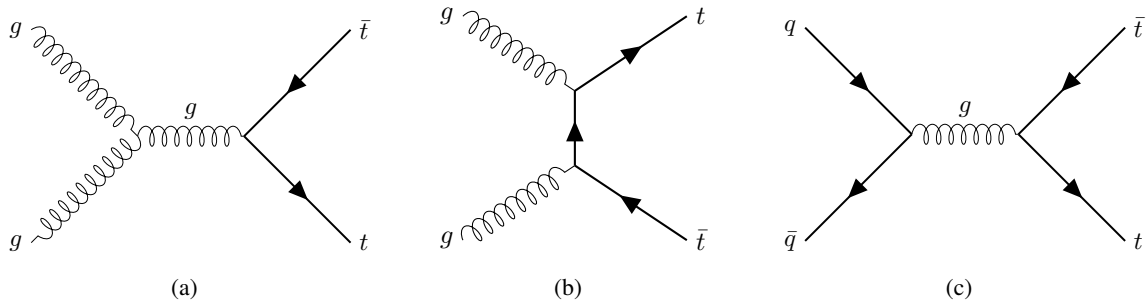


Figure 2.2: Leading order Feynman diagrams for $t\bar{t}$ production via the strong interaction at the LHC

Top quarks can also be produced singly in electroweak processes. The production processes are classified by the virtuality of the W boson exchanges in the process. The most abundant single top-quark production process at the LHC is t-channel production, followed by the associated production of a top quark and a real W boson, and s-channel production. Leading order diagrams of these processes are shown in figure 2.3. The production cross-section of these processes at LHC by the ATLAS collaboration is shown in figure 2.3(d). At the Tevatron, t-channel and s-channel single top-quark production are predicted by the SM, while Wt contribution is negligible [14].

By moving to next-to-leading order (NLO) electroweak production, there can be added to the single top processes, the radiation of a Z boson. This production process for which the total cross-section is

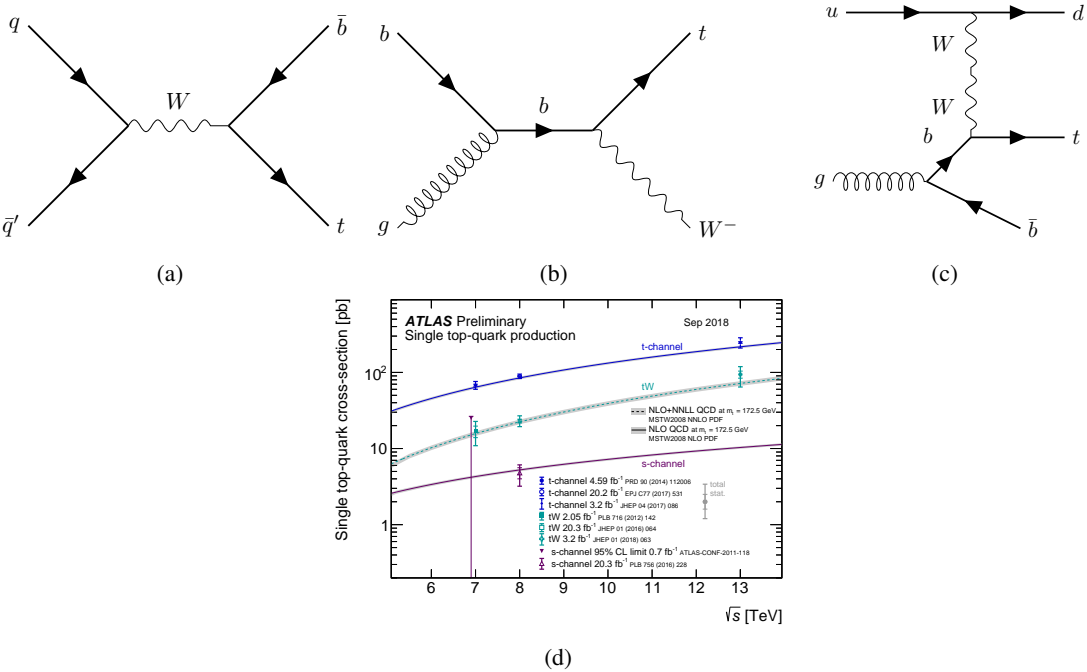


Figure 2.3: Feynman diagrams for single top quark production in the (a) s-channel, (b) in association with a W boson (c) t-channel production in 4FS , (d) measured single top quark production in ATLAS [15]

measured in this thesis consists of a top quark, a forward-jet and a Z boson at the parton level. The top quark is produced via the t-channel and the Z boson is either radiated off from one of the participating quarks or produced via W boson fusion. The Feynman diagrams of the tZq process at the leading order are shown in figure 2.4. As can be seen from figures 2.4(a) and 2.4(e), tZq production offers access to the coupling of the top quark to a Z boson and additionally to the WWZ coupling. Measuring this process is therefore a very interesting test of the SM, since the production rate could be modified by several BSM theories (e.g. in vector-like quark models).

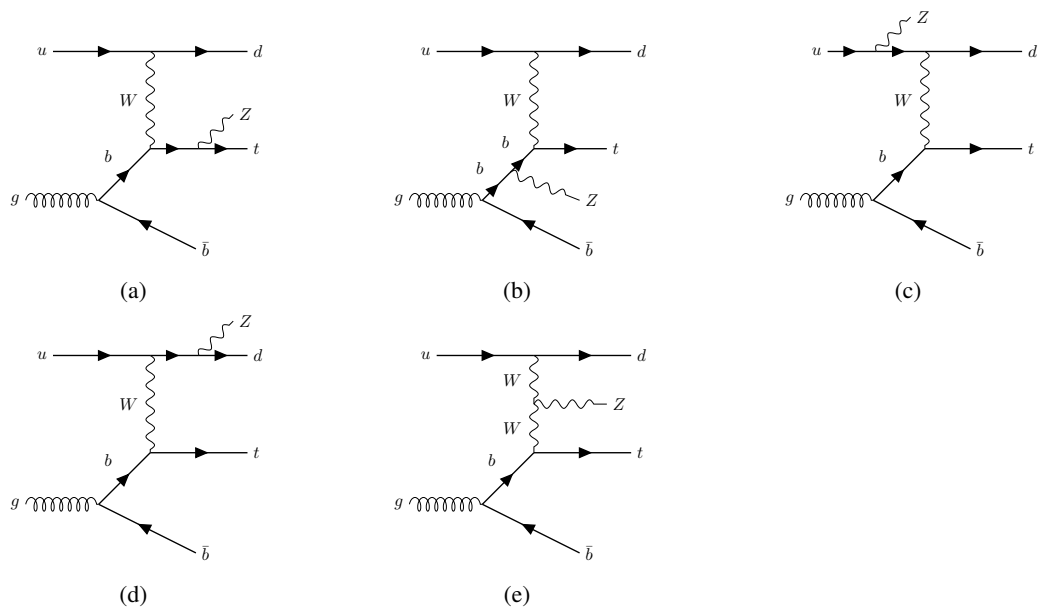


Figure 2.4: Feynman graphs to calculate the lowest order amplitudes of the tZq process. In the four-flavour scheme, the b-quark originates from gluon splitting..

CHAPTER 3

The LHC and the ATLAS experiment

In this chapter, the overall experimental setup is discussed. The Large Hadron Collider (LHC) which is the world's largest and the most powerful particle accelerator is discussed in section 3.1. Furthermore, the main setup of the ATLAS detector, which is one of the two general-purpose detectors at the LHC is discussed in section 3.2.

3.1 The LHC

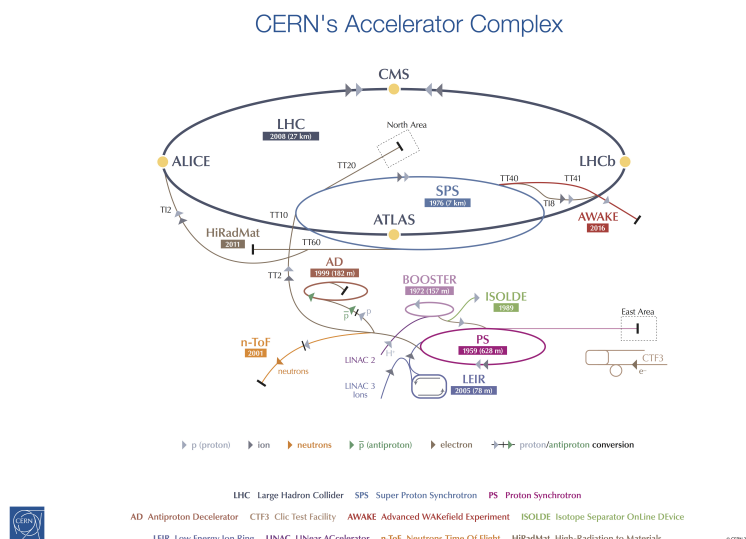


Figure 3.1: The CERN Accelerator Complex and its pre-accelerator chain as well as the location of the four main experiments[16]. The LHC is the large blue ring, which is fed from its predecessor the Super Proton Synchrotron (SPS), shown in light blue, in turn fed from its own predecessor the Proton Synchrotron (PS), in magenta.

The **Large Hadron Collider** (LHC), located at the European Organization for Nuclear Research (CERN), is largest and most energetic particle collider ever constructed. It is currently operating at a

record center-of-mass energy (\sqrt{s}) of 13 tera-electron-Volts (TeV) for proton-proton (pp) collisions. It allows scientists to reproduce the conditions that existed within a billionth of a second after the Big Bang by colliding beams of high-energy protons or ions at colossal speeds, close to the speed of light. Figure 3.1 gives an overview of the CERN accelerator complex. The LHC consists of a 27-kilometer ring of superconducting magnets with a number of accelerating structures to boost the energy of the particles along the way. Inside the accelerator, the particles are accelerated in opposite directions in two rings before they are made to collide. Before the particles are injected inside the beam pipes, they are injected into a linear accelerator (Linac 2) and are accelerated to an energy of 50 MeV. During this first acceleration, the protons are split into bunches. Then, they are injected into the Proton Synchrotron Booster (PSB). From there, the protons are led to the Proton Synchrotron (PS) with an energy of 1.4 GeV. Their energy is further increased to 25 GeV, and they are then injected to the Super Proton Synchrotron (SPS). Finally, the proton bunches pass to the LHC ring with an energy of 450 GeV, where they are accelerated to the desired energy. During Run I, the LHC operated at a center-of-mass energy of $\sqrt{s}=7$ TeV (2011) and at $\sqrt{s}=8$ TeV (2012). For Run II (2015-2018), the energy was increased to 13 TeV. The beams inside the LHC are made to collide at four locations around the accelerator ring, corresponding to the positions of four particle detectors ATLAS, CMS, ALICE and LHCb (see figure 3.1). The ATLAS and CMS detectors are cylindrically symmetrical multi-purpose detectors, which investigate a wide range of physics, from the search for the Higgs boson to extra dimensions and particles that could make up dark matter.

3.2 The ATLAS detector

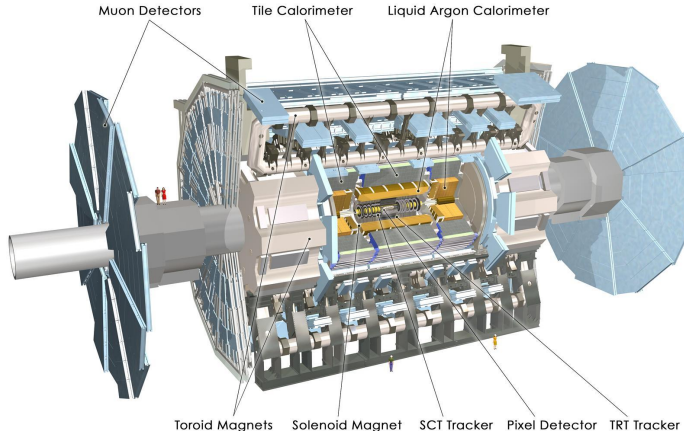


Figure 3.2: Overview over the entire ATLAS detector and its components [17]

The ATLAS detector (**A** **T**oroidal **L**HC **A**pparatu**S**) is one of the two largest particle detectors located at the LHC with a length of 44 meters, a diameter of 25 meters and 7000 tonnes of weight as shown in figure 3.2. It is the detector that is used to take the data for the analysis presented in this thesis and will also be assumed for the detector simulation of the Monte Carlo samples. The different detecting subsystems are arranged in layers around the collision point to record the paths, momentum, and energy of the particles, allowing them to be individually identified. It consists of three main detector components: the inner detector, the calorimeter system, and the muon spectrometer as shown

in figure 3.2. Additionally, the inner detector contains several toroidal and solenoidal magnets whose purpose is to bend charged particles (see figure 3.2). Charged particles such as leptons, charged mesons or charged hadrons can be detected through a combination of inner detector tracking and calorimeter deposits. Photons, neutral mesons or neutral hadrons can be identified due to their deposits in calorimeter paired with missing curved tracking information from the inner detector. Neutrinos do not interact with the detector components and are inferred by summing all transverse momentum to determine a "missing" energy. A schematic diagram of different particles interacting with the detector components is shown in figure 3.3.

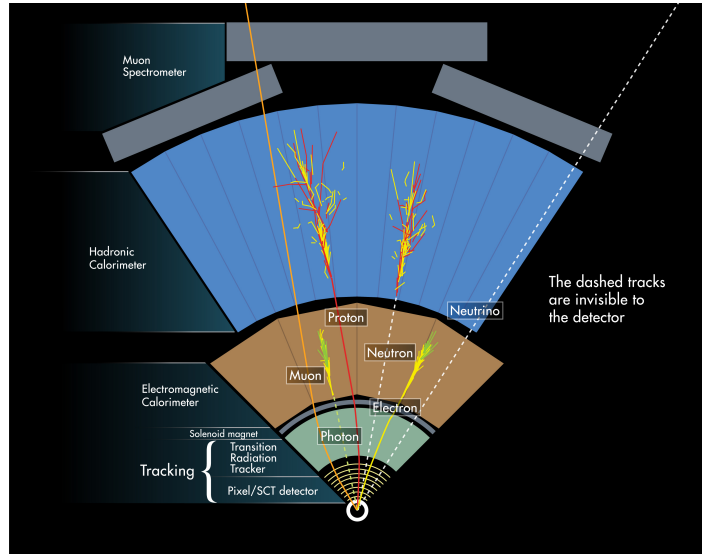


Figure 3.3: Depiction of the detectable particles upon a cross section of the ATLAS detector. [18]

3.2.1 The ATLAS coordinate system

ATLAS makes use of a right-handed coordinate system. The coordinate system has its origin at the nominal interaction point, with the z-axis pointed along the beamline. The x-y plane is transverse to the beam direction, with the positive x-axis pointing towards the center of the LHC ring and the positive y-axis defined as pointing upwards. Due to the symmetry, cylindrical coordinates are used, where ϕ is the angle along the plane transverse to the beam with respect to the x-axis and θ is the polar angle. Instead of the polar angle, pseudorapidity is used, which is defined as

$$\eta = -\ln(\tan \frac{\theta}{2}) \quad (3.1)$$

The distance between two particles or objects in the η - ϕ plane is defined as

$$\Delta R = \sqrt{(\Delta\eta)^2 + (\Delta\phi)^2} \quad (3.2)$$

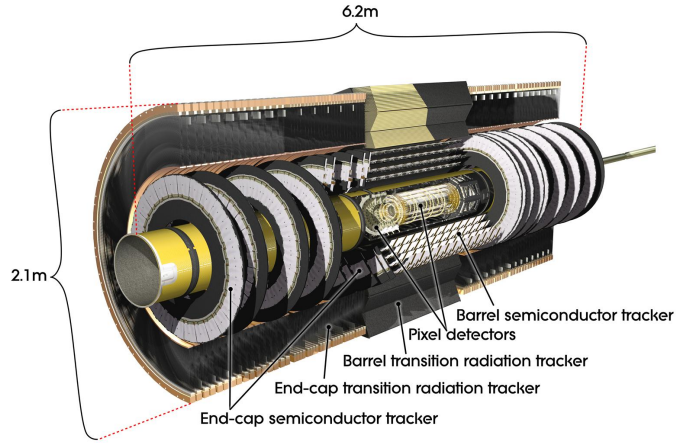


Figure 3.4: Cut-away view of the ATLAS inner detector [19]

3.2.2 Inner detector

The inner detector is the compact and highly sensitive part of the ATLAS detector that is used to measure the direction, momentum, and charge of electrically-charged particles produced in each proton-proton collision. It consists of three different systems of sensors, all immersed in a magnetic field of 2 T produced by a solenoid located between the tracking system and the calorimeter, parallel to the beam axis. The magnetic field bends the tracks of charged particles allowing a measurement of their momentum. The main components of the inner detector are Pixel Detector, Semiconductor Tracker (SCT), and Transition Radiation Tracker (TRT) as shown in figure 3.4.

The pixel detector is the inner part of the detector which is divided into barrel part and an end-cap region covering the range of $|\eta| < 2.5$. The barrel region starts 5 cm away from the interaction point making it the detector subsystem closest to the beam pipe. There are four barrel layers with 1736 sensor modules. In the end-cap region, each site constitutes three detector discs oriented perpendicular to the beam pipe with 288 modules. The individual module consists of pixels with size of $50 \times 400 \mu\text{m}^2$ in the external layers and $50 \times 250 \mu\text{m}^2$ in the innermost layers. Thus the pixel detector plays an important role in the reconstruction of primary and secondary vertices, the latter being useful information for b-tagging.

SCT consists of stereo silicon strips forming four concentric cylinders and nine end-cap discs on each side. It consists of a total of almost 16000 strip sensors, each 6.4 cm long and having an $80 \mu\text{m}$ pitch. It helps in simultaneous measurement of R and ϕ . TRT is the outer-most part of the inner detector that helps in precision measurement and provides an additional information on the particle type (pions or electrons) that flew through the detector. It consists of thin straw tubes with a diameter of 4 mm, which contain a 0.03 mm thin gold-plated tungsten wire in the centre. They are filled with a gas mixture of Xe, CO_2 , and O_2 .

3.2.3 Calorimetry

The calorimeter system of the ATLAS detector is divided into 2 subsystems, the inner electromagnetic calorimeter (EMcal) and the outer hadronic calorimeter (Hcal). Both the calorimeters are composed

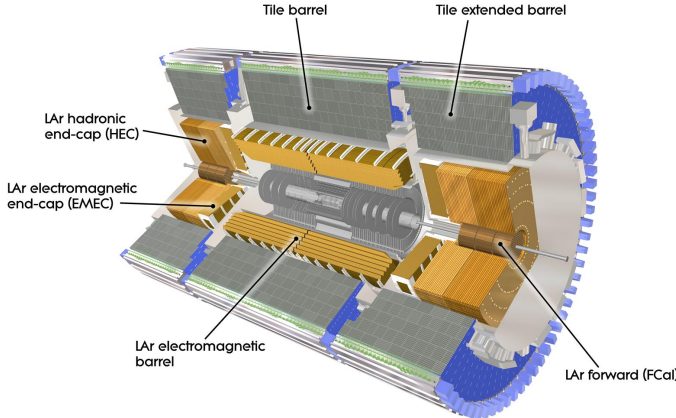


Figure 3.5: Cut-away view of the ATLAS calorimeter [20].

of multiple layers, alternating between an absorber material, which induces particle reactions leading to so called showers and an easy ionizable active material to detect the particles emerging from the absorber material. An overview of the ATLAS calorimeter is shown in figure 3.5 .

EMcal measures the deposited energy of electrons and photons. It is divided into a barrel part and two end-caps. Lead is used as absorber material while liquid argon (LAr) is used as active medium. A combined tile calorimeter and two sample calorimeters in the end-cap regions are used as Hcal. Hcal measures the deposited energy of hadrons. Here, copper is used as active material and LAr as active material. The energy resolution of the calorimeter system can be parametrised as

$$\frac{\sigma(E)}{E} = \frac{a}{\sqrt{E(GeV)}} \oplus b \quad (3.3)$$

For the electromagnetic calorimeter, the corresponding parameters are the stochastic term $a \approx 10\%$ and the constant $b \approx 0.7\%$, reflecting local non-uniformities in the calorimeter response. For the hadronic calorimeter, the parameters are $a \approx 50\%$ and $b \approx 3\%$ in the barrel and end-cap parts.

3.2.4 Muon system

Muons are the only SM particles besides neutrinos that escape the inner detector and calorimeters. Muon spectrometer is the outermost layer of the ATLAS detector. It detects muons and measures the properties of their tracks bent in the torodial magnetic field, using high-precision tracking chambers. It is made up of 4,000 individual muon chambers. It measures the paths of the muons that pass through over a total area the size of a footbal field, to an accuracy of less than one-hundredth of a millimeter. The muon spectrometer is also responsible for the enormous size of the ATLAS detector.

3.2.5 Trigger system

The ATLAS trigger system selects data in a way that the event at hand contains physics process of interest for the analysis. It consists of the hardware-based level-1 trigger (L1) and the software-based high-level trigger (HLT). Starting with a rate of proton-proton collision events of approximately

40 MHz is reduced to nearly 1 kHz after passing the event filter. The L1 uses a small amount of information from the calorimeters and muon spectrometer to look for objects and subsequently, regions of interest are built. The HLT is able to access full event data and analyses the regions of interest defined by the L1. After deciding whether to keep the event or not, the events are recorded for physics analysis after passing the event filter.

3.3 Physics objects reconstruction in ATLAS

In this section, the physics objects that are presented in this thesis is discussed. Electrons, muons, jets, bjets and missing transverse momentum are considered as physics objects. Their definitions are as follow

3.3.1 Electrons

Electron candidates are identified using a likelihood-based multivariate method which takes information about the energy deposit in the electromagnetic calorimeter and inner detector tracks. The energy deposit clusters are required to have transverse energy $E_T > 15$ GeV and be found in the pseudorapidity range $|\eta| < 2.7$ region, excluding the transition region between the barrel and end-cap EMcal found between $1.37 < |\eta| < 1.52$. The transverse impact parameter has to fulfill $|d_0/\sigma(d_0)| < 5$ and $|z_0 \sin(\theta)| < 0.5$ mm. Here d_0 and z_0 refer to the transverse and longitudinal distance of closest approach between the track and the primary vertex. Three quality requirements are available, in order of increasing background rejection power: LooseLH, MediumLH and TightLH. For this analysis all electron candidates are required to pass the TightLH¹ working point. Beyond the quality cut, electrons are required to be isolated using working point discussed in section 5.1.2

3.3.2 Muons

Muons are identified by the reconstruction of tracks in the inner detector and the muon spectrometer. To increase background rejection, some additional requirements are placed placed on track-parameter quality in the order of increasing background rejection power: Loose, Medium and Tight. They also have to fulfil $|d_0/\sigma(d_0)| < 3$ and $|z_0 \sin(\theta)| < 0.5$ mm. Muon candidates for this analysis pass the Medium identification working point.

3.3.3 Jets

Jets which represent cascades of matter generated in the process of quark hadronization are reconstructed from topological calorimeter clusters using the anti- k_t algorithm with a radius parameter of 0.4. They are required to have $P_T > 25$ GeV and $|\eta| < 4.5$. To suppress jets from pile-up, the Jet Vertex Tagger (JVT) is used.

3.3.4 B-jets

Identifying b-jets, which are jets from hadrons containing bottom quarks, is crucial for analyses with top quarks, since the top quark decays in almost 100% of all cases into a W boson and a bottom quark.

¹ Tight is used for this analysis as electron candidates quality.

B-jets are identified with the DL1r algorithm. Specially DL1r_PC variant is used; correspeng to the current recommendation. The chosen working point is 70% due to the optimal signal to background ratio.

3.3.5 Missing transverse energy

Missing transverse momentum E_T^{miss} is defined as the magnitude of the transverse momentum vector which quantifies the transverse momentum imbalance of all detectable momenta. Since neutrinos will pass the ATLAS detector without interacting with any of its sub-detectors, events containing neutrinos will contain E_T^{miss} due to energy-momentum conservation. The E_T^{miss} is calculated as the magnitude of the negative sum of the transverse momenta of all identified jets, electrons and muons in the event, as well as soft term built from tracks that are associated to the hard-scatter vertex but are not associated to any of the reconstructed objects.

CHAPTER 4

Data and Monte Carlo simulated events

4.1 Data sample

The analysis presented in this thesis uses data collected from 2015 to 2018 by the ATLAS detector at a center-of-mass energy of 13 TeV. The selected data periods were collected during stable beam LHC operations and with the ATLAS detector fully functioning. The total integrated luminosity is 139 fb^{-1} . Figure 4.1 shows the total integrated luminosity over time. The considered data events have been recorded by either electron or muon trigger. There were later filtered using so-called the Good Run List (GRL), which requires that the LHC beam has conditions to qualify it for physics analysis and is shown in blue in figure 4.1.

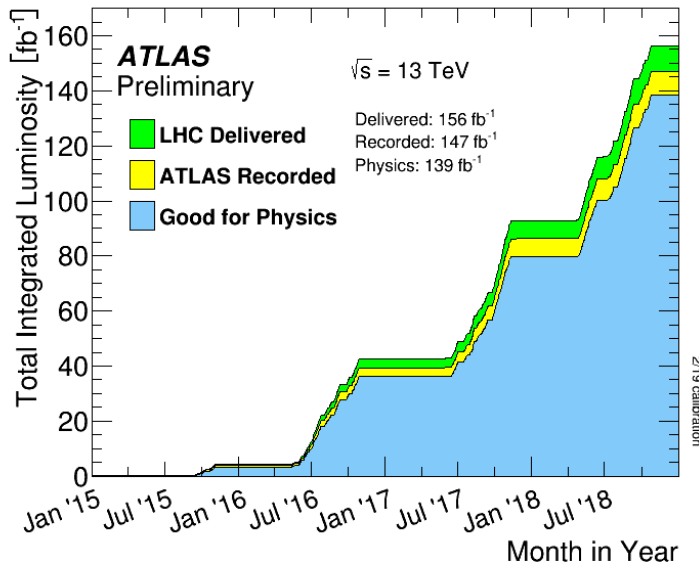


Figure 4.1: Cumulative luminosity versus time delivered to ATLAS (green), recorded by ATLAS (yellow), and certified to be good quality data (blue) during stable beams for pp collisions at 13 TeV centre-of-mass energy in 2015-2018 [21]

4.2 Monte Carlo simulation

Monte-Carlo (MC) simulation is an inevitable component of the ATLAS experiment in order to simulate all physics processes considered in the analysis. Because MC events are used to validate the analysis procedures to calculate the acceptance for the signal channel and to evaluate the contributions from the background processes. The MC simulation is divided into three steps [22]: The first is the detector independent generation of collision events which can be done by various external MC event generators interfaced by the ATLAS software framework Athena [23]. The event generation of the MC simulation includes the parton shower and hadronization process. The ~~next~~ *next* step of the MC simulation is the detector simulation, where a realistic picture of the energy deposit in the sensitive parts of the detector is simulated. The GEANT4 [24] toolkit is used to perform this simulation. It relies on the detector geometry, which describe physics constructions and conditions (e.g. magnetic field, alignment of detectors parts, dead read-out channels) of the detector. The last step of the MC simulation of all events is the digitization of the simulation hits. At this step, the energy deposited inside the sensitive part of the detector is translated to an increase of a voltage or an electric current in a given read-out channel with further digitization of this analog electronic signal. The output of digitization is recorded in so-called digits. Digits are inputs for further emulation of the detector read-out electronics, Read Out Drives (ROD); which produce the so called Raw Data Objects (RDO). RDOs are the inputs for the offline reconstruction of physical objects. After the digitization step, the MC simulated events and data are equivalently treated by the event reconstruction algorithms.

All the above described major steps of the MC simulation are brought together in the simulation software of the Athena framework. Further processing of the simulated events implies reconstruction for the physics results.

4.2.1 Signal sample

The tZq sample is simulated using the MadGraph5_aMC@NLOv2.3.3 [25] generator at NLO with NNPDF3.0NO parton distribution function (PDF). The four flavor scheme is used where all the quark masses are set to zero, except for the top and bottom quarks. The SM $t l^+ l^- q$ MC sample used in the analysis (DSID:412063) contains a trilepton filter. The top quark decays as expected in the SM, $t \rightarrow b W$. Only the leptonic decay of the W boson is considered.

4.2.2 Background sample

Several SM processes are expected to have the same final-state particles as the signal events and are considered as a background to the tZq trilepton analysis. The event signature which has been searched consists of a high p_T b-quark, three-charged leptons (μ, e) and missing transverse energy (E_T), from the neutrino of the semi-leptonic W boson decays. The main backgrounds are therefore WZ, ZZ, $t\bar{t}$, Z+jets, $t\bar{t}Z$, tWZ etc.

Details of all simulated samples are given in table 4.1.

Process	MC generator	Parton shower	PDF set	Order
WZ	SHERPA 2.1.1 [26, 27]	SHERPA	CT10	
ZZ	SHERPA 2.1.1	SHERPA	CT10	
$t\bar{t}$	POWHEG [28]	Pythia 6 [29]	CT10	
tW	POWHEG	Pythia 6	NNPDF2.3LO	
Z+jets	POWHEG	Pythia 6	NNPDF2.3LO	
$t\bar{t}Z$	MadGraph5_aMC@NLO	Pythia 8 [30]	NNPDF2.3LO	
tWZ	MadGraph5_aMC@NLO	Pythia 8	NNPDF2.3LO	

Table 4.1: Overview of background MC generated samples.

4.2.3 Reweighting of Monte-Carlo simulated events

The number of events generated during the MC simulations generally do not exactly match the number of expected events for a given physical process at a given integrated luminosity. Each MC event is given a weight to rescale it so that the overall MC sample accurately represents the physical processes. Thus, to correctly reproduce the data-taking conditions, as well as replicate the efficiency of selecting different physics objects, in the simulated samples, event-by-event correction factors are applied to the MC events. The total event weight can be written as:

$$w_{\text{event}} = w_{\text{MC}} \times w_{\text{pile-up}} \times w_{\text{lepton}} \times w_{\text{JVT}} \times w_{\text{trigger}} \times w_{\text{b-tagging}} \quad (4.1)$$

The term w_{MC} is the MC event weight. The $w_{\text{pile-up}}$ term is introduced to the MC samples, as a certain pile-up profile is assumed during MC simulation where as w_{lepton} term is related to the efficiency of reconstructing, identifying a certain lepton. The w_{trigger} term is related to the trigger. The final state considered for analysis consists of a b-tagged jet, thus $w_{\text{b-tagging}}$ weight is applied.

4.2.4 Luminosity reweighting

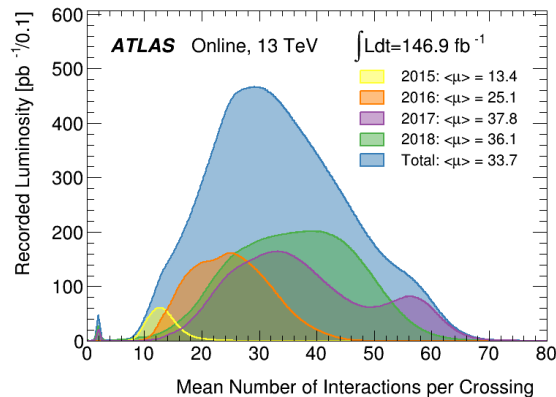


Figure 4.2: Luminosity weighted plot of the mean number of interactions per crossing for the 2015 and 2016 datasets [21].

The signal and background processes are simulated with large statistics. Thus, the luminosity for the MC simulated samples are very high. In order to correctly match the process to a dataset, the luminosity of the MC sample is scaled. The weight or scale factor is defined as

$$w_{lumi} = \frac{\sigma_{process}}{N} \mathcal{L} \quad (4.2)$$

$\sigma_{process}$ is the cross-section of the specific physical process. \mathcal{L} is the integrated luminosity of the data sample and N is the number of events in the original MC sample.

CHAPTER 5

Events selection

The goal of the event selection is to achieve the highest possible fraction of tZq events in data as predicted by Monte-Carlo Simulation. Data events are selected if they pass the preselection criteria discussed in Section 4.1. The preselection treatments are also applied on MC events. In order to verify the modeling of physics processes in the relevant areas of kinematic phase space, a set of signal, and control regions are defined. Each region is defined by a set of selection cuts on the reconstructed variables. These reconstructed variables can also be the one from intermediate-state particles which are calculated from the final state observables.

5.1 Signal region

As shown in the Feynman diagrams in 2.4, the tZq signal consists of a top quark, a forward-jet and a Z boson. The final state at the leading order for which the analysis is performed consists of three leptons, one neutrino, one b-quark and a light quark which is expected in the forward direction. The two of the three leptons come from the Z decay and the one from the leptonic W decay.

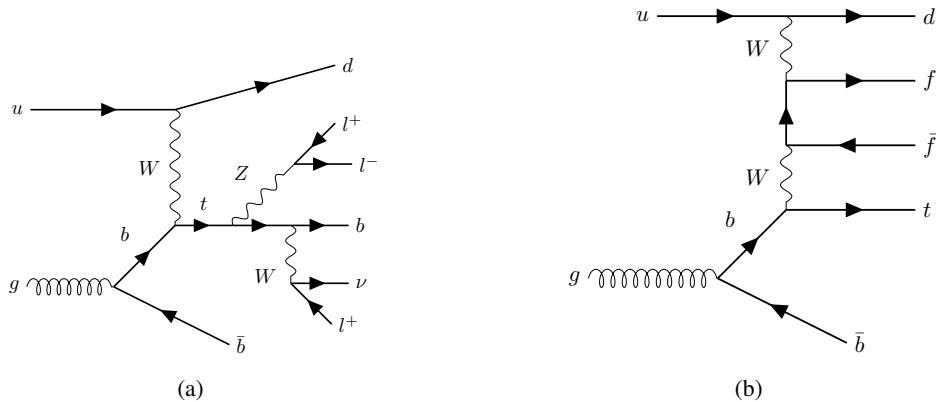


Figure 5.1: Leading order Feynman diagrams with the trilepton final state. (a) resonant production of dilepton pairs, (b) non-resonant production of dilepton pairs

The trilepton final state at the leading order is shown in Feynman diagrams 5.1. The signal has also contributions from the non-resonant dilepton production as in figure 5.1(b). The QCD calculations at

NLO suggests that there can exist significant QCD radiation present in the event which can manifest itself in the form of a third reconstructed jet.

In order to increase acceptance as much as reasonably possible two orthogonal signal regions (SRs) named as *SR-2j1b* and *SR-3j1b* are defined. In SR-2j1b, events with three leptons, one b-tagged jet and one untagged jet as forward jet are selected. In SR-3j1b, events are selected identically to the SR-2j1b except for the inclusion of a second untagged jet. One of the two untagged jets, that one that gives, with the b-jet, the highest invariant mass, m_{bj_f} is selected to be the forward jet. The remaining jet is called radiation jet. The same nomenclature is used for the jets in the control regions (CRs)

5.1.1 Full event reconstruction

From the final states of the process, the variables are reconstructed. The reconstructed variables are the ~~one~~^{ones} directly measured in the detector or the intermediate one, calculated from the final state observables. In order to reconstruct the Z boson, an opposite-sign, same-flavor (OSSF) lepton pair is needed. In the $ee\mu$ and $e\mu\mu$ channels, this is uniquely identified. For the eee and $\mu\mu\mu$ events, both possible combinations are considered and the pair that has the invariant mass closest to the Z boson mass is chosen.

The remaining lepton and the missing momentum from neutrino is used to reconstruct the W boson. The missing part of the neutrino four-vector is the longitudinal component along the z-axis (P_z^ν), which can be obtained using the mass constraint of the W boson which is M_W , 80.4 GeV. The reconstruction is taken from the Ref. [31]. From the four-momentum conservation

$$(P^W)^2 = (P^l + P^\nu)^2 = M_W^2 \quad (5.1)$$

The solution of the quadratic equation given in eqn. 5.1 in terms of the P_z^ν can be expressed as follows

$$P_z^\nu = \frac{\alpha \cdot P_z^l \pm \sqrt{(E^l)^2(\alpha^2 - P_T^l \cdot \vec{E}_T)}}{(P_T^l)^2} \quad (5.2)$$

where α is given by

$$\alpha = \frac{M_W^2}{2} + \vec{P}_T^l \cdot \vec{E}_T \quad (5.3)$$

when the quantity under the square root is positive ($\alpha^2 \geq P_T^l \cdot \vec{E}_T$), then there are two real solutions, and the smallest one in magnitude is taken. Since the W boson is expected to be produced with small rapidity. For some events, eqn. 5.1 has imaginary solution ($\alpha^2 \leq P_T^l \cdot \vec{E}_T$), which is interpreted as a mis-measurement of \vec{E}_T . In this case the transverse mass, $m_T(W)$, is greater than M_W and $m_T(W)$ is explicitly set to equal M_W and the neutrino 4-vector is rescaled. Technically this is resolved by introducing a new scale factor β , which is defined by

$$\beta = \frac{M_W^2}{2P_T^l} \cdot \vec{E}_T - \vec{P}_T^l \cdot \vec{E}_T \quad (5.4)$$

β is used to scale E_x , E_y and E_T and then α is recalculated as shown in eqn. 5.3. P_z^ν is found by considering only the offset part of the eqn. 5.2.

Then, the reconstructed W boson and the b-tagged jet are used for the t-quark reconstruction as

follows

$$P^t = P^W + P^{b\text{-jet}} \quad (5.5)$$

A summary of relevant symbols representing the reconstructed objects is presented in table 5.1

Symbol	Description
l_1^Z	Highest p_T lepton from the reconstructed Z boson
l_2^Z	Lowest p_T lepton from the reconstructed Z boson
Z	Reconstructed Z boson
l^W	Lepton from the reconstructed W boson from the t-quark decay
W	Reconstructed W boson from the t-quark decay
b-jet	b-tagged jet
t	Reconstructed t quark
j_f	Forward jet
j_r	Radiation jet
$l_{1/2/3}$	p_T ordered leptons
$j_{1/2/3}$	p_T ordered jets

Table 5.1: Object reconstruction.

5.1.2 Lepton isolation working point

In order to reduce the contribution of the background processes from the non-prompt leptons, the isolation working points are studied. For details on isolation working point Ref. [32] can be referred.

Name	Electron	Muon
Gradient	Gradient	FCTightTrackOnly_FixedRad
PLV	PLVTight	PLVTight
PLVLoose	PLVLoose	PLVLoose
PLIV	PLImprovedTight	PLImprovedTight
PLIVV	PLImprovedVeryTight	PLImprovedVeryTight
Pflow	PflowTight	PflowTight_VarRad
TrackOnly	TightTrackOnly	TightTrackOnly_VarRad
Tight	Tight	Tight_VarRad

Table 5.2: Combination of the Isolation Working Point analysed

In this analysis, the yield for a set of isolation WPs shown in the table 5.2 is presented. The yield are obtained with the following selection cuts: The three leptons are sorted by their p_T , irrespective of flavour, and required to have transverse momenta of at least 28, 20 and 20 GeV, respectively. Jets are required to have $P_T > 35$ GeV with one b-tagged jet with 70% WP.


 Figure 5.2: Relative yield for SR 2j1b with jet $p_T > 35$ GeV, lepton $p_T > 28, 20, 20$, GeV & btag-eff: 70%

 Figure 5.3: Relative yield for SR 3j1b with jet $p_T > 35$ GeV, lepton $p_T > 28, 20, 20$, GeV & btag-eff: 70%

5.1 Signal region

Figure 5.2 and 5.3 shows the relative yield for the different lepton WPs. It is found that PLV, PLIV, and PLIVV have large signal and small fake-background compared to others. While PLVLoose has comparatively large fake background. The significance calculated in table 5.3 shows that PLVLoose has the highest significance for both SR-2j1b and SR-3j1b. The significance is also high for PLV and PLIV compared to others. So, the lepton WPs: PLV, and PLVLoose are chosen for the optimization of selection cuts.

Lepton WPs	SR 2j1b			SR 3j1b		
	S	B	$\frac{S}{\sqrt{S+B}}$	S	B	$\frac{S}{\sqrt{S+B}}$
Gradient	89.40	230.38	5.00	50.89	200.73	3.21
PLV	83.73	182.51	5.13	47.67	174.82	3.20
PLVLoose	91.50	209.26	5.28	52.10	193.61	3.32
PLIV	80.70	171.8	5.08	46.10	168.10	3.15
PLIVV	66.50	140.90	4.62	38.30	139.10	2.88
Pflow	79.86	180.27	4.95	45.79	170.38	3.11
TrackOnly	92.59	240.56	5.07	52.61	209.22	3.25
Tight	81.82	186.88	4.99	46.96	176.06	3.14

Table 5.3: Values of the Significance for SR 2j1b and SR 3j1b for various Isolation WPs

5.1.3 Optimization of cuts

The analysis aims to set new requirements on the phase space so that the contribution of the signal grows relative to the number of background events. The significance is calculated for different selection cuts and are compared to the previous selections used in Ref. [31]. The cuts are optimized by varying leptons p_T , jets p_T and the b-tagging efficiency of the b-tagged jet.

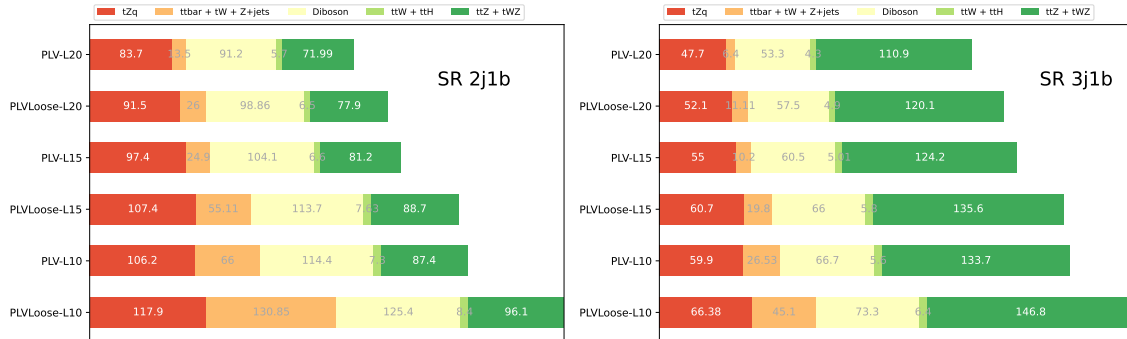


Figure 5.4: Yield for signal and background at varying third lepton p_T

Figure 5.4 shows the yield at varying third lepton p_T , while the first and third lepton p_T remain at 28 GeV and 20 GeV respectively. The btagging WP is 70% and the jet transverse momentum remain above 30 GeV. It shows that both the signal and background increases with loose third lepton p_T cut. The significance in table 5.4 that PLV at 10 GeV and PLVLoose at 15 GeV have considerable signal to background ratio while significance is above 5σ for SR-2j1b and 3σ for SR-3j1b (Figure 5.6)

Lepton WPs	$p_T(\ell_3) >$	SR 2j1b			SR 3j1b		
		S	B	$\frac{S}{\sqrt{S+B}}$	S	B	$\frac{S}{\sqrt{S+B}}$
PLV	20 GeV	83.70	182.39	5.13	47.7	174.9	3.20
	15 GeV	97.40	216.80	5.49	55.00	199.91	3.44
	10 GeV	106.40	275.10	5.45	59.90	232.53	3.50
PLVLoose	20 GeV	91.50	209.26	5.28	52.10	193.61	3.32
	15 GeV	107.40	265.14	5.56	60.7	227.20	3.58
	10 GeV	117.90	360.75	5.35	66.38	271.60	3.61

 Table 5.4: Significance calculated at varying third lepton p_T for both SR-2j1b and SR-3j1b

shows that the change in the first lepton p_T from 28 GeV to 27 GeV does not change the yield much for both PLV and PLVLoose. Similarly the yield remains same by changing the second lepton p_T from 20 GeV to 15 GeV. Thus, the final cut for analysis for the leptons p_T are set to 27, 20, 10 GeV for PLV and 27, 20, 15 GeV for PLVLoose for first, second and third lepton p_T respectively.

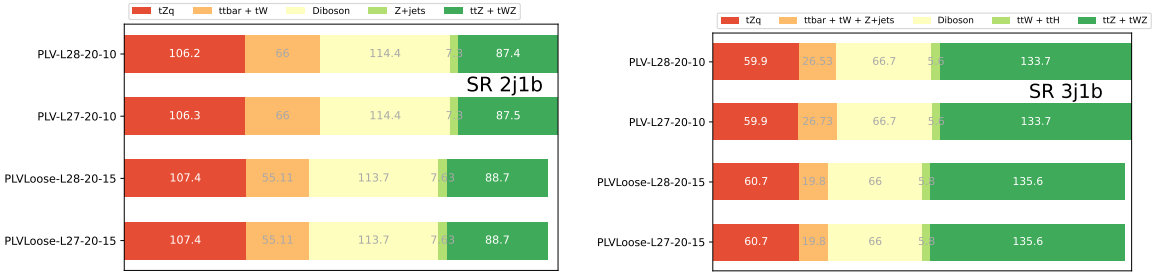
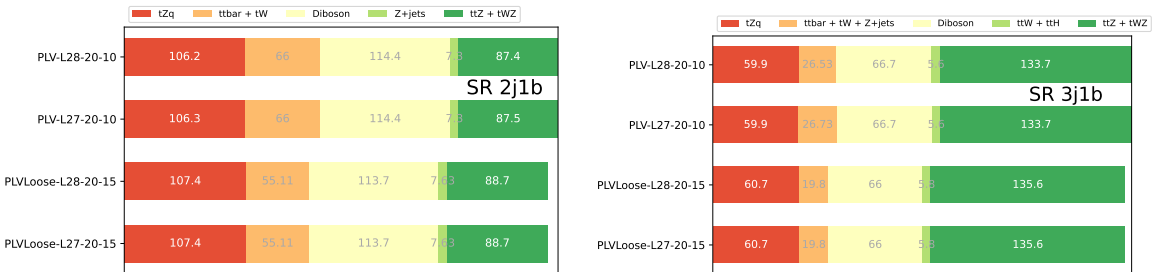

 Figure 5.5: Events yeild for signal and background at varying first lepton p_T

 Figure 5.6: Events yeild for signal and background at varying second lepton p_T

Figure 5.7 and 5.8 shows the yield at varying jet p_T , b-tagging efficiency and third lepton p_T . The lower in jet p_T migrate the signal to higher jet multiplicity keeping total number of signal in SR-2j1b and SR-3j1b nearly same. There is large increase in diboson background yield with increase in b-tagging working point. Here, in the plot the diboson contribution is split according to the origin of the associated jets using generator-level information. If one of the jets contains a b- or c-hadron then it

5.1 Signal region

is classified as diboson + heavy flavour (VV + HF), otherwise the event is classified as diboson + light flavour (VV + LF). Thus for final cut for the jet transverse momentum and b-jet tagging efficiency for our analysis remain at 35 GeV and 70%.



Figure 5.7: Events yeild for signal and background obtained by varing the jet p_T , b-tagging efficiency and the third lepton p_T in the SR-2j1b



Figure 5.8: Events yeild for signal and background obtained by varing the jet p_T , b-tagging efficiency and the third lepton p_T in the SR-3j1b

5.1.4 Signal regions (SRs) plots and yields

The regions are constructed as described in section 5.1. The full selection cuts applied in the signal regions are listed in table 5.5. In this table, the selection cuts for the definition of control regions are also reported. The event yields in the SRs after the full selection can be found in table 5.6 and histogram distributions of reconstructed variables from the top quark and Z boson are given in figure

Common selections			
Exactly 3 leptons (e or μ) with $ \eta < 2.5$			
$p_T(\ell_1) > 27 \text{ GeV}$, $p_T(\ell_2) > 20 \text{ GeV}$, $p_T(\ell_3) > 10 \text{ GeV}$			
$p_T(\text{jet}) > 35 \text{ GeV}$			
SR 2j1b	CR Diboson 2j0b	CR $t\bar{t}Z$ 3j2b	CR $t\bar{t}$ 2j1b
≥ 1 OSSF pair	≥ 1 OSSF pair	≥ 1 OSSF pair	≥ 1 OSDF pair
$ m_{\ell\ell} - m_Z < 10 \text{ GeV}$	$ m_{\ell\ell} - m_Z < 10 \text{ GeV}$	$ m_{\ell\ell} - m_Z < 10 \text{ GeV}$	No OSSF pair
2 jets, $ \eta < 4.5$	2 jets, $ \eta < 4.5$	3 jets, $ \eta < 4.5$	2 jets, $ \eta < 4.5$
1 bjet, $ \eta < 2.5$	0 bjets	2 bjets, $ \eta < 2.5$	1 bjet, $ \eta < 2.5$
SR 3j1b	CR Diboson 3j0b	CR $t\bar{t}Z$ 4j2b	CR $t\bar{t}$ 3j1b
≥ 1 OSSF pair	≥ 1 OSSF pair	≥ 1 OSSF pair	≥ 1 OSDF pair
$ m_{\ell\ell} - m_Z < 10 \text{ GeV}$	$ m_{\ell\ell} - m_Z < 10 \text{ GeV}$	$ m_{\ell\ell} - m_Z < 10 \text{ GeV}$	No OSSF pair
3 jets, $ \eta < 4.5$	3 jets, $ \eta < 4.5$	4 jets, $ \eta < 4.5$	3 jets, $ \eta < 4.5$
1 bjet, $ \eta < 2.5$	0 bjets	2 bjets, $ \eta < 2.5$	1 bjet, $ \eta < 2.5$

Table 5.5: Overview of the requirements applied when selecting events in the signal and control regions. OSSF is an opposite-sign same-flavour lepton pair. OSDF is an opposite-sign different-flavour lepton pair.

5.9. The predicted number of events to pass selection cuts based on MC simulations for tZq as well as all previously mentioned backgrounds are tabulated. The events in these regions are the primary regions of interest for the statistical analysis described in section 6.4 after having been evaluated by the neural network described in section 6.2.

Process	Number of events	Number of raw events	Process	Number of events	Number of raw events
tZq	97.46 ± 0.67	56838800	tZq	55.31 ± 0.56	38569200
$t\bar{t}$	22.72 ± 0.88	104389	$t\bar{t}$	10.79 ± 0.61	49206
tW	0.89 ± 0.61	1112	tW	0.33 ± 0.58	417
$Z+jets$	36.66 ± 4.13	228516	$Z+jets$	13.32 ± 1.14	102582
Diboson	115.60 ± 1.09	5741400	Diboson	66.05 ± 0.70	3615390
$t\bar{t}Z$	62.88 ± 2.30	7001290	$t\bar{t}Z$	101.39 ± 0.68	12441100
$t\bar{t}W$	4.56 ± 0.18	255621	$t\bar{t}W$	2.34 ± 0.13	134969
$t\bar{t}WZ$	19.34 ± 0.58	489419	$t\bar{t}WZ$	22.92 ± 0.65	596449
$t\bar{t}H$	2.11 ± 0.04	715711	$t\bar{t}H$	2.80 ± 0.05	753658
Total expected	362.22 ± 4.65	71376200	Total expected	275.24 ± 1.84	56262900
Data	443	443	Data	307	307

Table 5.6: Numbers of expected events in the SR-2j1b (Left) and SR-3j1b (Right) broken down by process. The uncertainty shown contains only the statistical component.

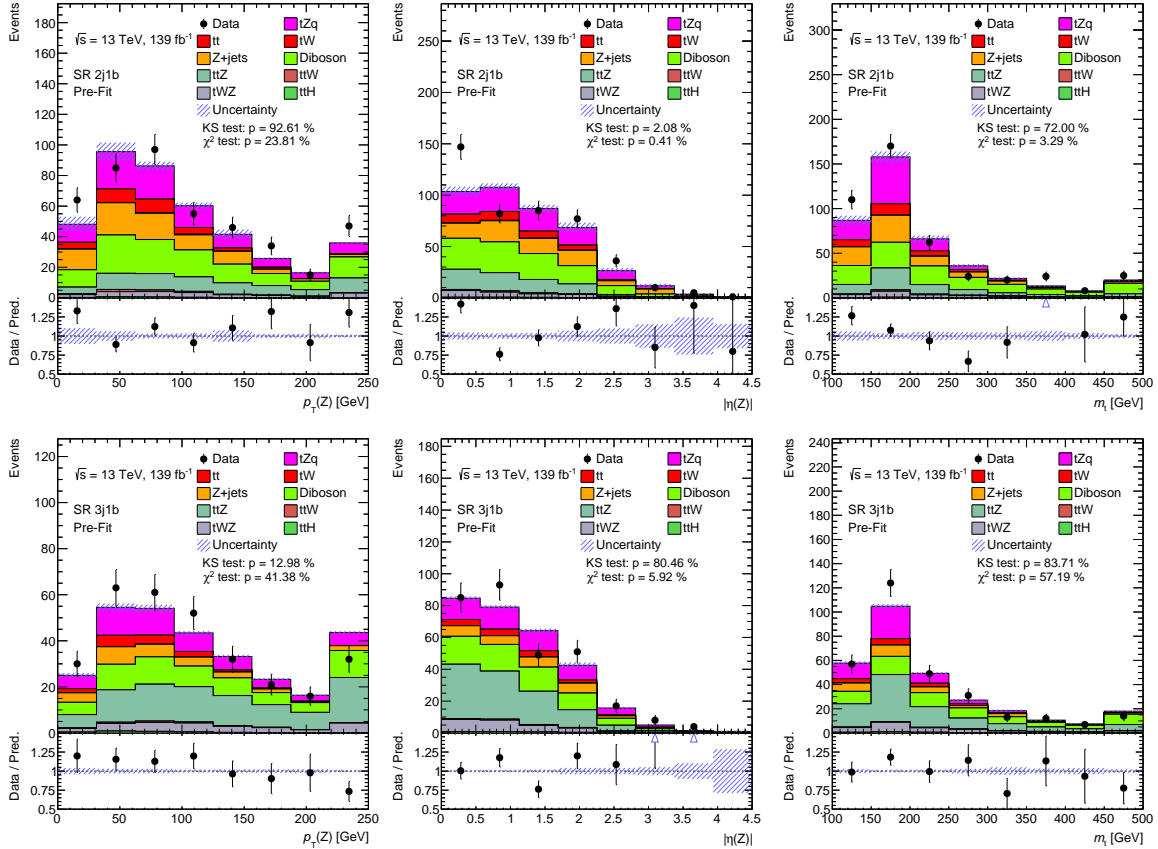


Figure 5.9: Comparison of data and MC predictions for reconstructed event-related quantities for events in the SR-2j1b and SR-3j1b. The uncertainty shown is the statistical uncertainty

5.2 Control regions (CRs)

In order to ensure proper modeling of each relevant background, a series of control regions as listed in table 5.5 are defined. These regions are constructed such that they are enriched in three of the main sources of backgrounds: diboson, $t\bar{t}Z$, and $t\bar{t}$ production. There are two CRs for each background, and one corresponding to each signal region.

5.2.1 Diboson CRs plots and yields

To define regions of phase space enriched in diboson production, the b-jet is vetoed. This leads to events such as WZ to dominate while effectively removing the events containing the top quark. This region also has significant contamination from Z+jets events.

The two diboson control regions are listed in table 5.5. The events yields in diboson CRs after the full section are shown in table 5.7. Some of the reconstructed variables in this control regions are shown in figure 5.10. The large number of observed events in this control region helps to provide a significant constraint on the overall rate of diboson events.

Process	Number of events	Number of raw events
tZq	61.94 ± 0.57	40215200
tt	14.58 ± 0.73	64357
tW	0.49 ± 0.75	556
Z+jets	152.32 ± 18.75	624666
Diboson	2625.59 ± 5.02	146163000
ttZ	48.59 ± 4.79	4766730
ttW	1.85 ± 0.11	98134
tWZ	17.10 ± 0.54	422977
ttH	1.14 ± 0.03	323175
Total expected	2923.59 ± 17.11	192679000
Data	3116	3116

Process	Number of events	Number of raw events
tZq	25.58 ± 0.42	21530100
tt	5.59 ± 0.46	24603
tW	0.60 ± 0.42	695
Z+jets	52.53 ± 5.89	244640
Diboson	973.45 ± 2.35	60037700
ttZ	47.15 ± 1.42	6095710
ttW	0.88 ± 0.09	51847
tWZ	13.13 ± 0.51	375439
ttH	1.07 ± 0.03	268270
Total expected	1119.97 ± 6.51	88629000
Data	1083	1083

Table 5.7: Numbers of expected events in the CR-2j0b (Left) and CR-3j0b (Right) broken down by process. The uncertainty shown contains only the statistical component.

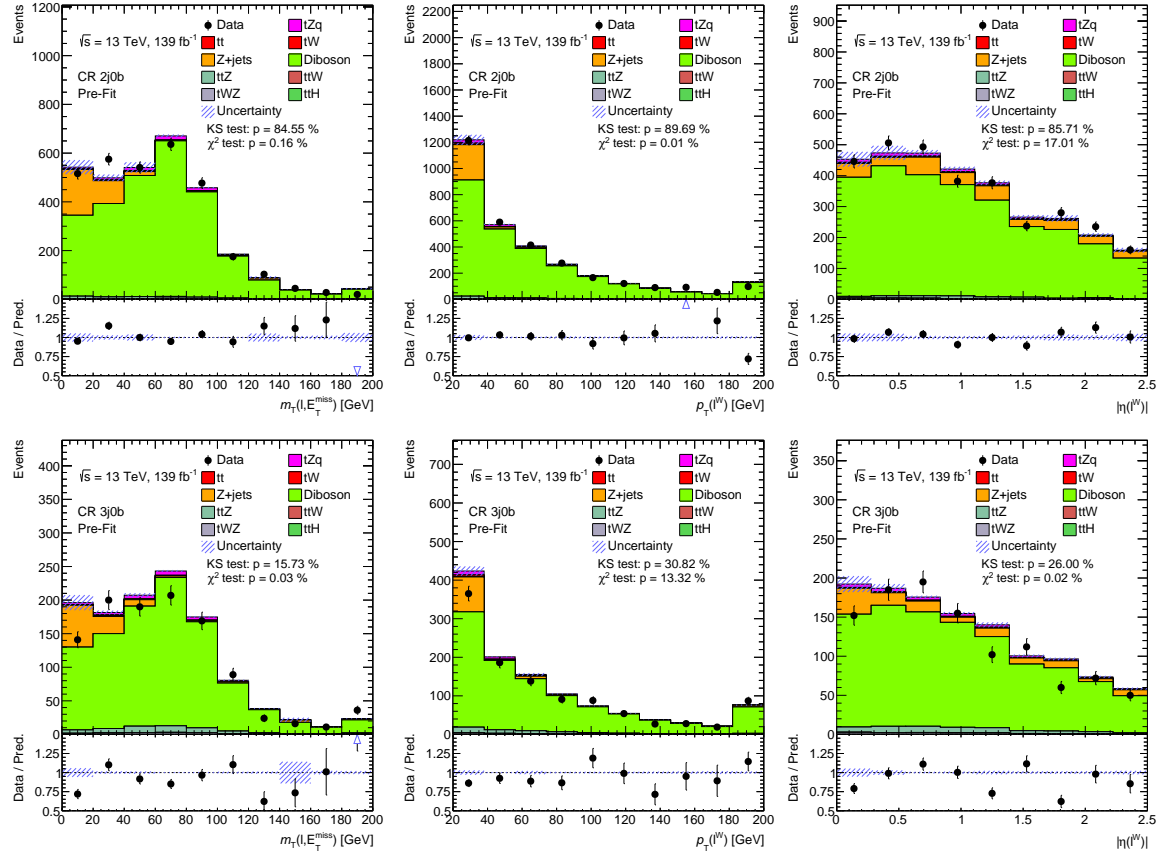


Figure 5.10: Comparison of data and MC predictions for reconstructed event related quantities for events in the CR 2j0b and CR 3j0b.

5.2.2 $t\bar{t}Z$ CRs plots and yield

To define regions of phase space enriched in $t\bar{t}Z$ production, an additional b-jet is required to enhance events with a second top quark. This region also contains significant amount of signal events.

Process	Number of events	Number of raw events	Process	Number of events	Number of raw events
tZq	15.78 ± 0.23	6584710	tZq	10.43 ± 0.20	5136470
tt	2.31 ± 0.30	11120	tt	1.14 ± 0.22	5699
tW	0.08 ± 0.43	139	tW	0.16 ± 0.38	278
Z+jets	1.10 ± 0.19	8062	Z+jets	0.56 ± 0.13	4170
Diboson	5.48 ± 0.16	381555	Diboson	3.38 ± 0.12	230184
ttZ	48.94 ± 0.45	5681490	ttZ	53.35 ± 0.51	7061060
ttW	1.69 ± 0.12	105501	ttW	0.76 ± 0.07	42812
tWZ	3.91 ± 0.26	100775	tWZ	4.76 ± 0.29	120652
ttH	1.59 ± 0.04	488446	ttH	1.41 ± 0.04	365153
Total expected	80.88 ± 0.70	13361800	Total expected	75.94 ± 0.68	12966500
Data	118	118	Data	77	77

Table 5.8: Numbers of expected events in the CR-3j2b (Left) and CR-4j2b (Right) broken down by process. The uncertainty shown contains only the statistical component.

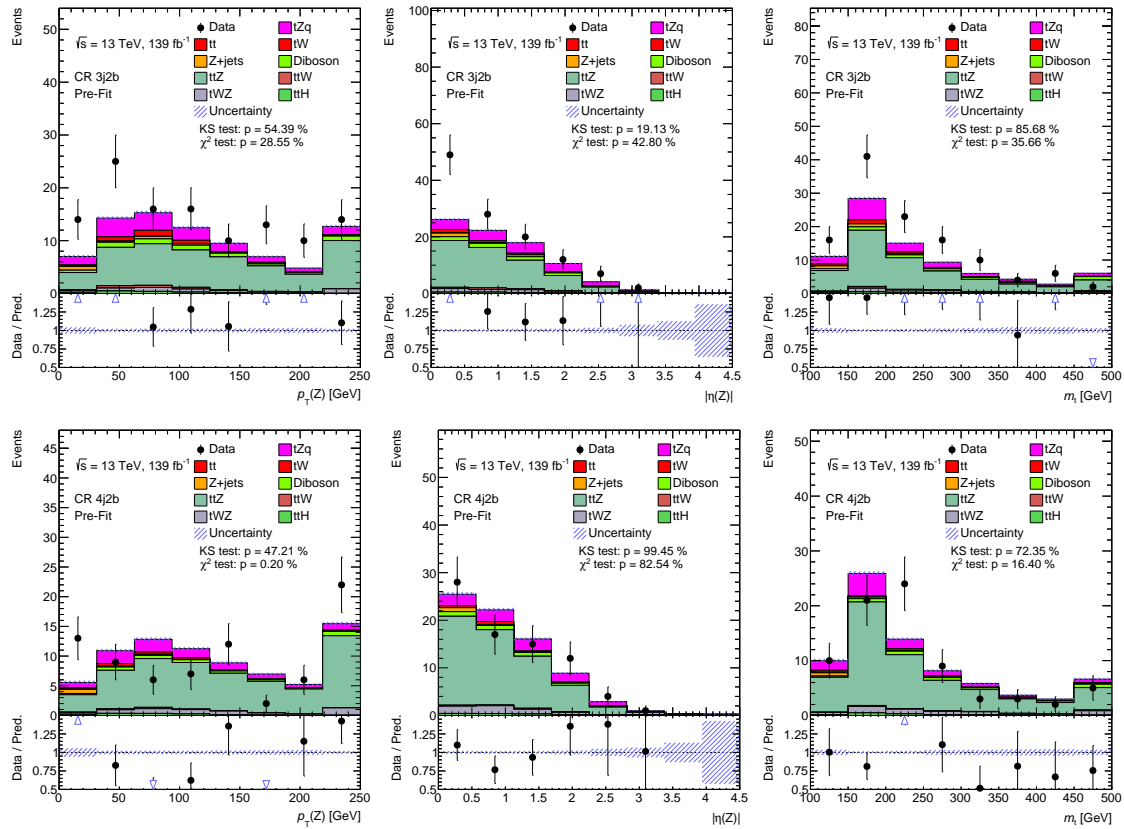


Figure 5.11: Comparison of data and MC predictions for reconstructed event-related quantities for events in the CR-3j2b and CR-4j2b. The uncertainty shown is the statistical uncertainty.



The two $t\bar{t}Z$ control regions are listed in Table 5.5. The events yields in $t\bar{t}Z$ CRs after the full section are shown in Table 5.8. Some of the reconstructed variables in this control regions are shown in figure 5.11.

The $t\bar{t}Z$ CRs are unique in that they require an extra b-jet which introduces an ambiguity in the event selection and reconstruction criteria. Here, only one of the b-jet is considered and other one is neglected. The forward jet is then selected as in Section 5.1. The $t\bar{t}Z$ CRs also have contamination from tZq signal events which can create a bias in the measurement. This is solved by fitting the neural-network output, O_{NN} distribution (Section 6.2) which shows separation between the tZq and $t\bar{t}Z$. This allows robust constraint of $t\bar{t}Z$ modeling and also a slight boost to the overall measurement's sensitivity.

5.2.3 $t\bar{t}$ CRs plots and yields

Finally, the $t\bar{t}$ contribution can be enhanced by requiring the OSSF lepton requirement be removed, effectively removing the requirement on the Z boson and opposite-sign, different-flavor (OSDF) leptons condition is imposed. This phase space is dominated by $t\bar{t}$ events with a fake lepton and a b-jet.

The two $t\bar{t}$ CRs are also defined in Table 5.5. The event yields in the $t\bar{t}$ CRs after the full selection can be found in Table 5.9 and reconstructed variables from the top quark and Z boson are given in Fig. 5.12.

The $t\bar{t}$ CRs suffer from the lowest statistics of all fitted regions. Because of this, two binned histograms per region is used in the statistical analysis.

Process	Number of events	Number of raw events	Process	Number of events	Number of raw events
tZq	0.34 ± 0.04	200994	tZq	0.21 ± 0.03	139834
$t\bar{t}$	43.40 ± 1.23	197797	$t\bar{t}$	20.27 ± 0.84	93408
tW	2.32 ± 0.52	3058	tW	1.06 ± 0.61	1251
$Z+jets$	0.19 ± 0.15	556	$Z+jets$	0.13 ± 0.13	417
Diboson	0.39 ± 0.07	21545	Diboson	0.30 ± 0.04	14178
$t\bar{t}Z$	2.69 ± 0.12	262293	$t\bar{t}Z$	2.47 ± 0.12	284950
$t\bar{t}W$	9.76 ± 0.26	494284	$t\bar{t}W$	5.19 ± 0.20	308302
$t\bar{t}WZ$	0.44 ± 0.10	12649	$t\bar{t}WZ$	0.26 ± 0.09	10981
$t\bar{t}H$	3.35 ± 0.05	1234180	$t\bar{t}H$	3.90 ± 0.06	1.222370
Total expected	62.87 ± 1.37	2427360	Total expected	33.80 ± 0.96	2075690
Data	71	71	Data	49	49

Table 5.9: Numbers of expected events in the CR-2j1b (Left) and CR-3j1b (Right) broken down by process. The uncertainty shown contains only the statistical component.

5.2 Control regions (CRs)

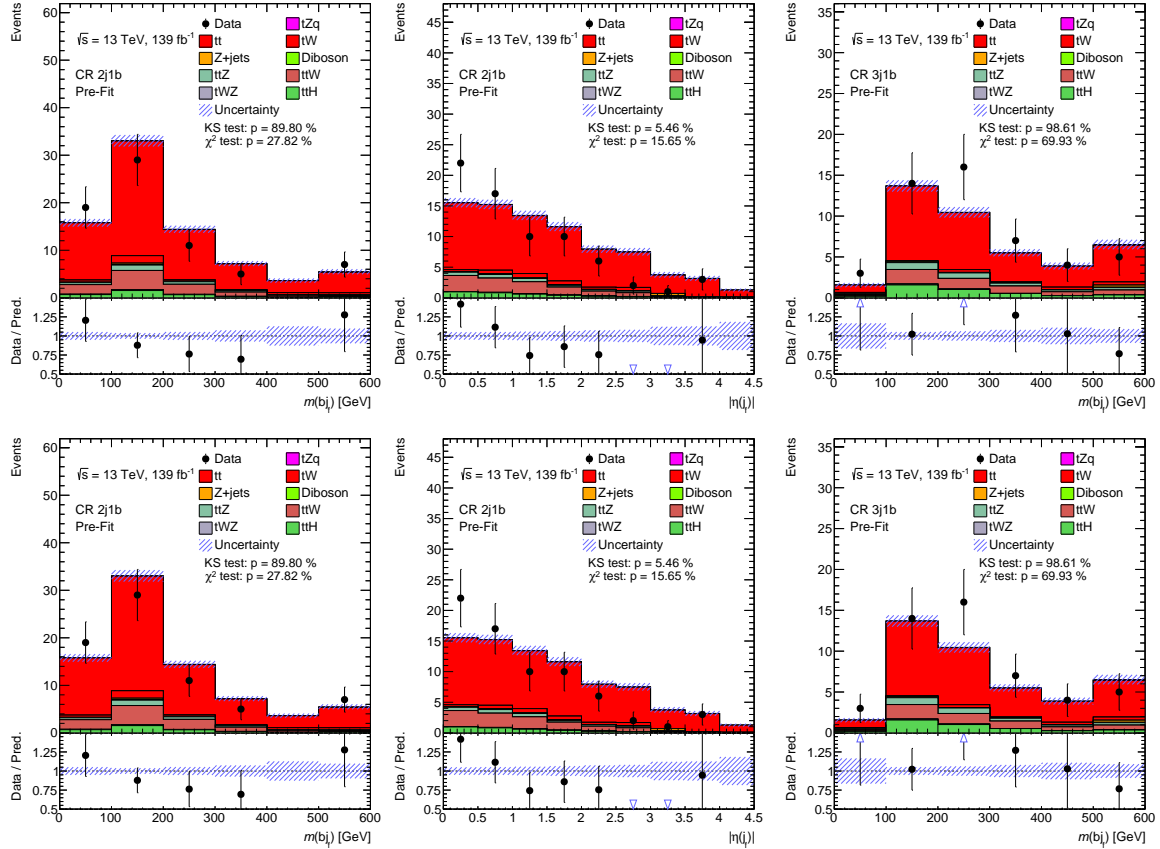


Figure 5.12: Comparison of data and MC predictions for reconstructed event-related quantities for events in the CR-2j1b and CR-3j1b. The uncertainty shown is the statistical uncertainty.

CHAPTER 6

Analysis

This chapter describes the setup that will be used in the final fit to the data and the expected signal and background events described in chapter 4.

Section 6.1 gives an overview of the fit used for extracting a cross-section measurement. Section 6.2 presents the signal and background separation procedure, where an artificial neural network is used as multivariate classification technique. Section 6.5 explain in short about the systematic uncertainties and the possible that can modify the rate of the signal and background process. Section 6.4 gives a basic idea of binned profile likelihood fit which is used is used for signal extraction in this thesis. Binning optimisation and a fit using Asimov fit is presented in section 6.5.4 to test the fit performance.

6.1 Cross-section measurement analysis strategy

The strategy of this analysis is to determine the signal strength μ_{tZq} (POI) of the tZq process, hence the total cross-section while including systematic uncertainties as nuisance parameter in the profile likelihood fit as described in Section 6.4. Two different signal regions as defined in section 5.1, with different amount of signal and background contributions, are used to determine μ_{tZq} . As defined in section 5.2, control regions are defined to determine the normalization of the respective dominant background processes. Both the signal and three backgrounds, $t\bar{t} + tW$ and $Z + \text{jets}$, & $t\bar{t}Z$ normalization factors are fitted as free parameters in all eight regions simultaneously. The contributions of all other backgrounds are set to their expected values and are allowed to vary within their systematic uncertainties, which are included as nuisance parameter in the fit. For the cross section of tZq , where the Z boson decays into the charged leptons (e^+e^- , $\mu^+\mu^-$), $\sigma_{t\bar{t}l^+l^-q} = 102$ fb is assumed to be the nominal value [31] for the fit. which corresponds to the signal strength of $\mu = 1$.

6.2 Signal and background separation

In order to separate the signal and background for the SM tZq processes, a cut-and-count analysis is difficult and will give bad sensitivity, due to the large number of background events and the big uncertainties associated to them. In high energy physics, multivariate analysis techniques such artificial neural networks (NN's) have been used or proposed as good candidates for tasks of signal versus background classification.

6.3 Multivariate analysis technique: Artificial Neural Network (NN)

An artificial neural network (NN) is a simplified mathematical structure inspired from the real biological neural networks. It has similar basic concepts of a real biological neural network (neuron, connection strength, input linearity, output-linearity) but in a much more conservative level of complexity. The neuron is a mathematical entity which has a real value depending on the connection strengths (weights) and the values of the other neurons with which it is connected. The non-linear function that relates the output from the neuron with the weights and the inputs to the neuron is usually called *activation function*. A neural network can be structured as layers. The input layer, from where the NN is fed with the input variables of the problem to be solved, followed by a number of layers called hidden layers, and finally the output layers.

An example of a multi-layer neural network is shown in figure 6.1 (b). It contains a layer of n input neurons X_i ($i=1, \dots, n$), with an activation function f_{X_i} , a hidden layer of m neurons H_j ($j=1, \dots, m$) with activation function f_{H_j} and an output layer of two neurons Y_p ($p=1, 2$) with activation function f_{Y_p} . The output node gives continuous output (O_{NN}) between 0 and 1, where the output tends to 0 for background, and +1 for signal. The neural network output is calculated as follows:

$$Y_p = f_{Y_p}(\zeta_{Y_p}) = f_{Y_p} \left(\sum_{j=1}^{m+1} w_{pj} f_{H_j}(\zeta_{H_j}) \right) = f_{Y_p} \left(\sum_{j=1}^{m+1} w_{pj} f_{H_j} \left(\sum_{i=1}^{n+1} v_{ji} f_{X_i}(X_i) \right) \right) \quad (6.1)$$

where w_{pj} are the weights between the input layer and the hidden layer, and v_{ji} are the weights between the hidden layer and the output layer.

In this analysis a supervised neural network with three-layer feed-forward algorithm is implemented using Tensflow in Python. Elu is used as activation function for both input and hidden layers whereas sigmoid for output layer. The response curve for elu and sigmoid can be seen in figure ??.

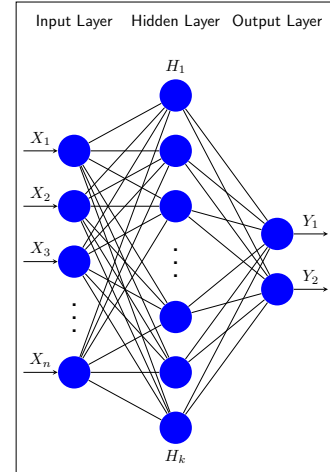
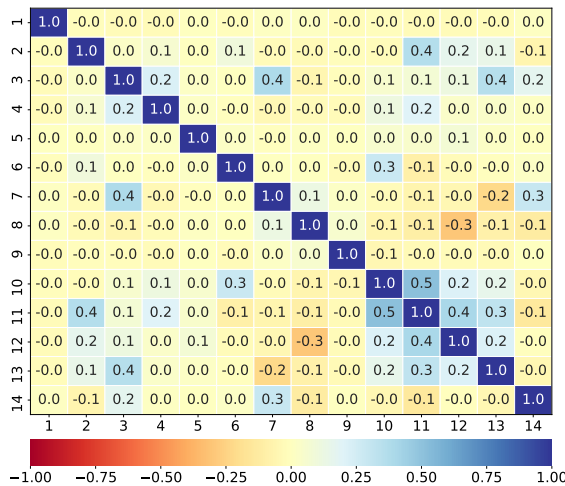


Figure 6.1: a) Correlation matrix between the different input variables. b) Final network configuration. Meaning of variables and numbers given in table 6.1

6.3.1 Input variables

The input variables are chosen in an iterative process. First, many variables are used to train preliminary NN. The correlations between variables in MC events are determined. In the second step, the relevant variables with the biggest separation power are investigated by comparing the MC distributions. The signal event signature is simple as defined in [Section 5.1](#). ~~Thus the input variables are limited ad~~ *and* can be categorized as: variables measured directly in the detector, others which are reconstructed from the measured quantities as described in [Section 5.1.1](#). All possible variables such as momenta, relative angles, pseudo-rapidity, and particle masses are explored. The variables used to train the NN in the SR 2j1b, SR 3j1b, CR 3j2b, and CR 4j2b are listed with their rank in [Table 6.1](#). The ranking of variables is done by creating a baseline classifier using all the input variables used for training with a simple network. The training is repeated as many times as there are variables in list but each training beyond the baseline replaces a variable by a uniform distribution. The classifiers with missing variables are compared with the baseline classifier by performing the t-test and one can then use the 'statistics' of the classifier as ranking.

Variable	Rank		Definition
	SR 2j1b	SR 3j1b	
m_{bj_f}	1	1	(Largest) invariant mass of the b-jet and the untagged jet(s)
m_t	2	2	Reconstructed top-quark mass
$p_T(W)$	3	3	p_T of the reconstructed W boson
$p_T(Z)$	4	4	p_T of the reconstructed Z boson
$p_T(j_f)$	5	5	p_T of the forward jet
$p_T(\ell_W)$	6	7	p_T of the lepton from the W-boson decay
m_Z	7	8	Mass of the reconstructed Z boson
$m_T(\ell, E_T^{miss})$	8	9	Transverse mass of the W boson
$ \eta(\ell_W) $	9	10	Absolute value of the η of the lepton from the W-boson decay
$ \eta(j_f) $	10	12	Absolute value of the η of the forward jet
$\Delta R(j_f, Z)$	11	14	ΔR between the forward jet and the reconstructed Z boson
b-tagging score	12	15	b-tagging score of the b-jet
$ \eta(Z) $	13	13	Absolute value of the η of the reconstructed Z boson
E_T^{miss}	14	16	Missing transverse momentum
$p_T(j_r)$	–	6	p_T of the radiation jet
$ \eta(j_r) $	–	11	Absolute value of the η of the j_r jet

Table 6.1: Variables used as input to the neural network in SR 2j1b and SR 3j1b. The ranking of the variables in each of the SRs is given in the 2nd and 3rd columns, respectively.

6.3.2 Data and MC comparison

Since the neural network is trained with simulated events, it is important to check if the input variables are modelled correctly. Data and MC distributions are compared in [figure 6.2, 6.3, 6.4, 6.5 and 6.6](#). All MC distributions are normalised using their predicted cross-section values.

Additionally, Kolmogorov-Smirnov test (KS-test) and Chi-Square (χ^2 -test) are performed for each distributions. The p-value obtained during the test is shown along with the distributions.

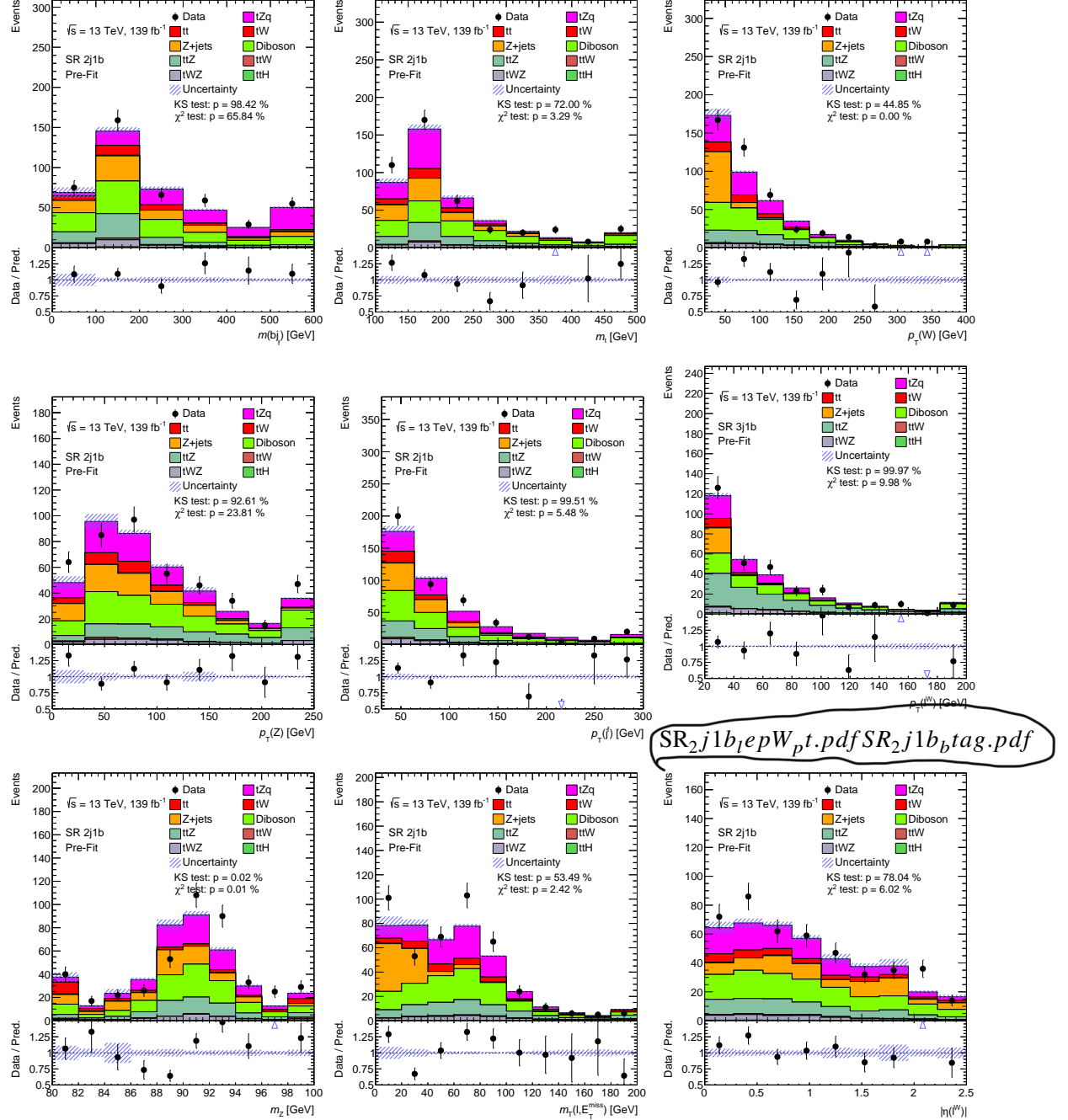


Figure 6.2: Stacked kinematic plots of neural-network training variables of the SR 2j1b, in order of significance. Both signal and backgrounds are normalised to the expected number of events before the fit. The uncertainty band includes statistical uncertainties for signal and backgrounds

6.3 Multivariate analysis technique: Artificial Neural Network (NN)

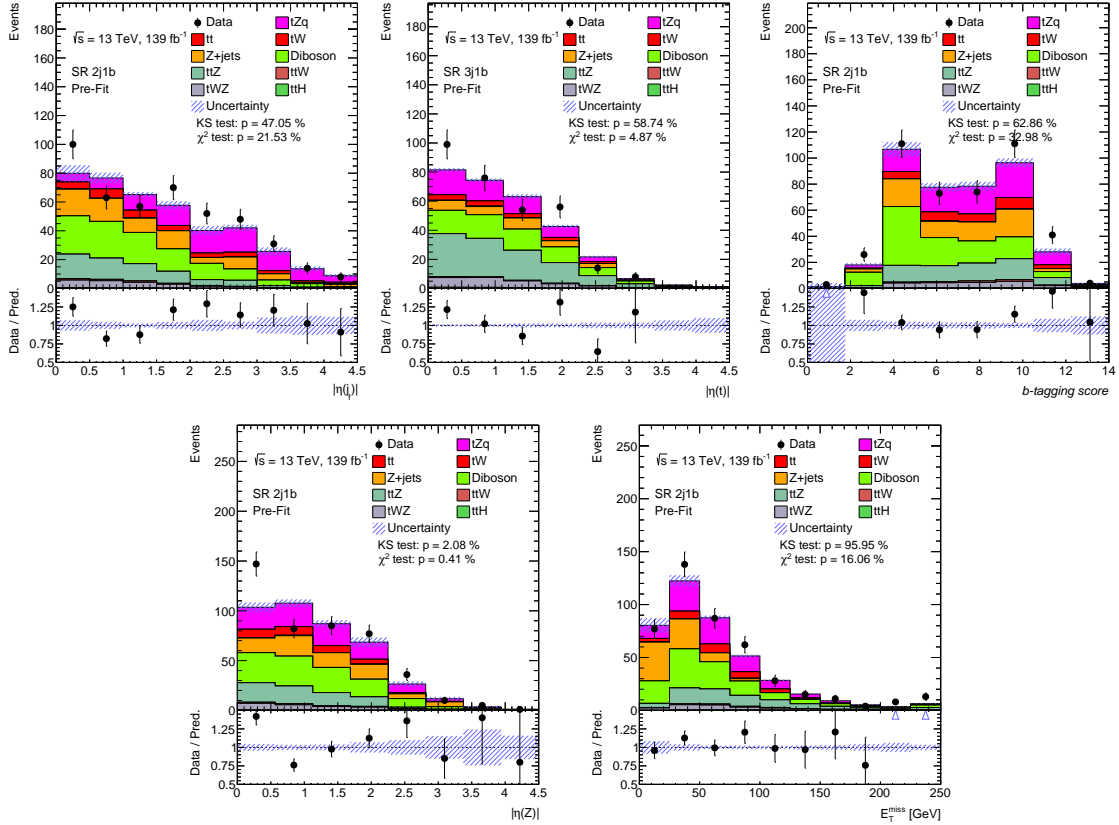


Figure 6.3: Stacked kinematic plots of neural-network training variables of the SR 2j1b, in order of significance. Both signal and backgrounds are normalised to the expected number of events before the fit. The uncertainty band includes statistical uncertainties for signal and backgrounds

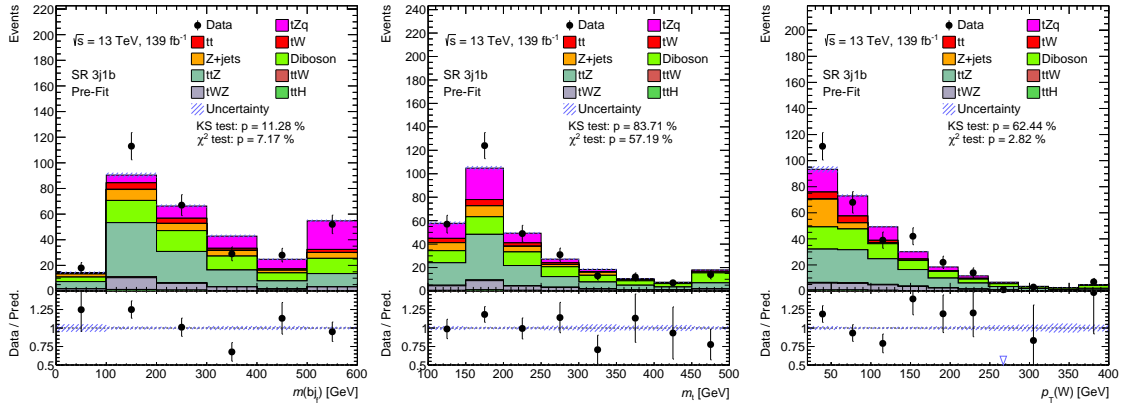


Figure 6.4: Stacked kinematic plots of neural-network training variables of the SR 3j1b, in order of significance. Both signal and backgrounds are normalised to the expected number of events before the fit. The uncertainty band includes statistical uncertainties for signal and backgrounds

Chapter 6 Analysis

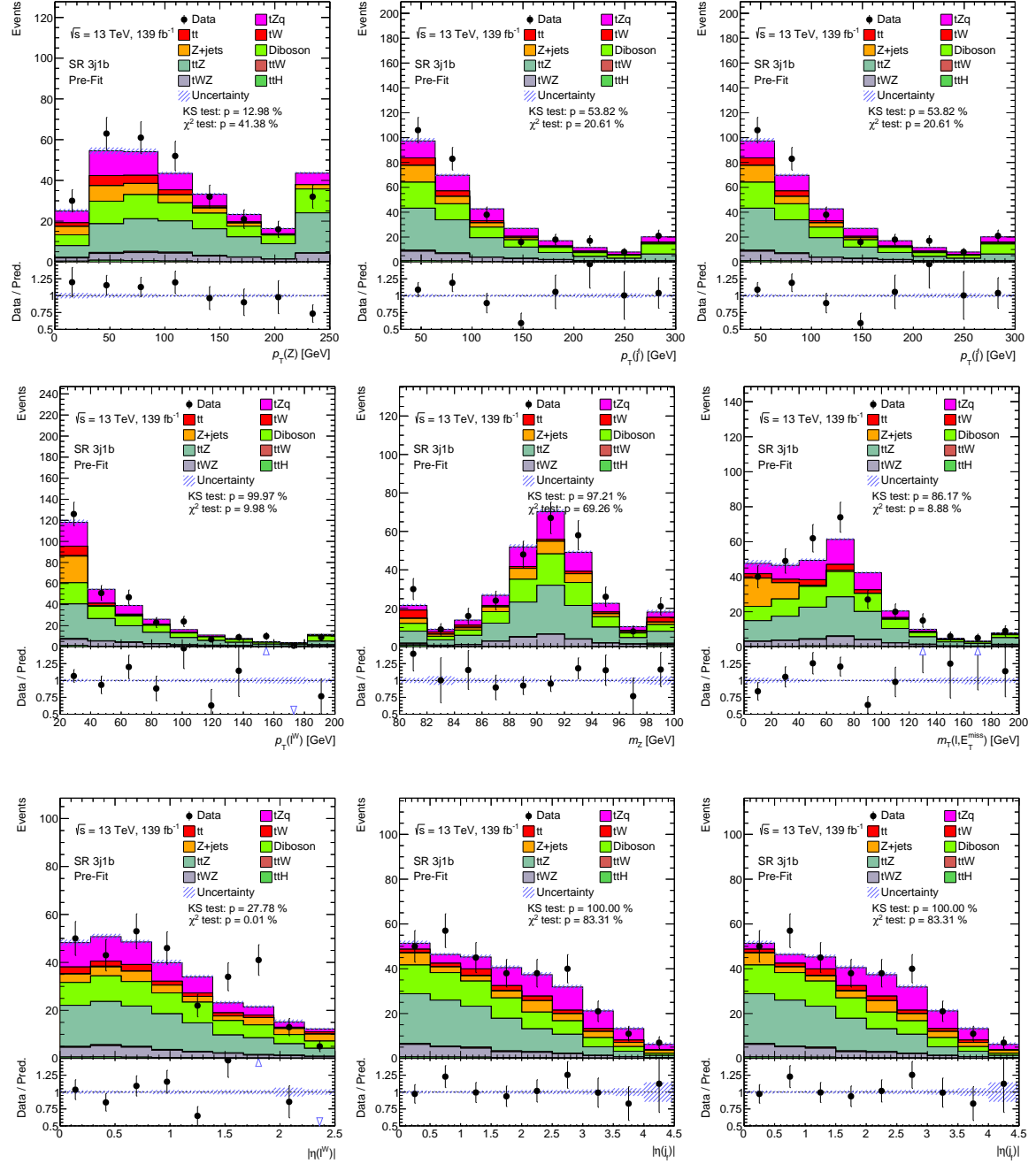


Figure 6.5: Stacked kinematic plots of neural-network training variables of the SR 3j1b, in order of significance. Both signal and backgrounds are normalised to the expected number of events before the fit. The uncertainty band includes statistical uncertainties for signal and backgrounds

6.3 Multivariate analysis technique: Artificial Neural Network (NN)

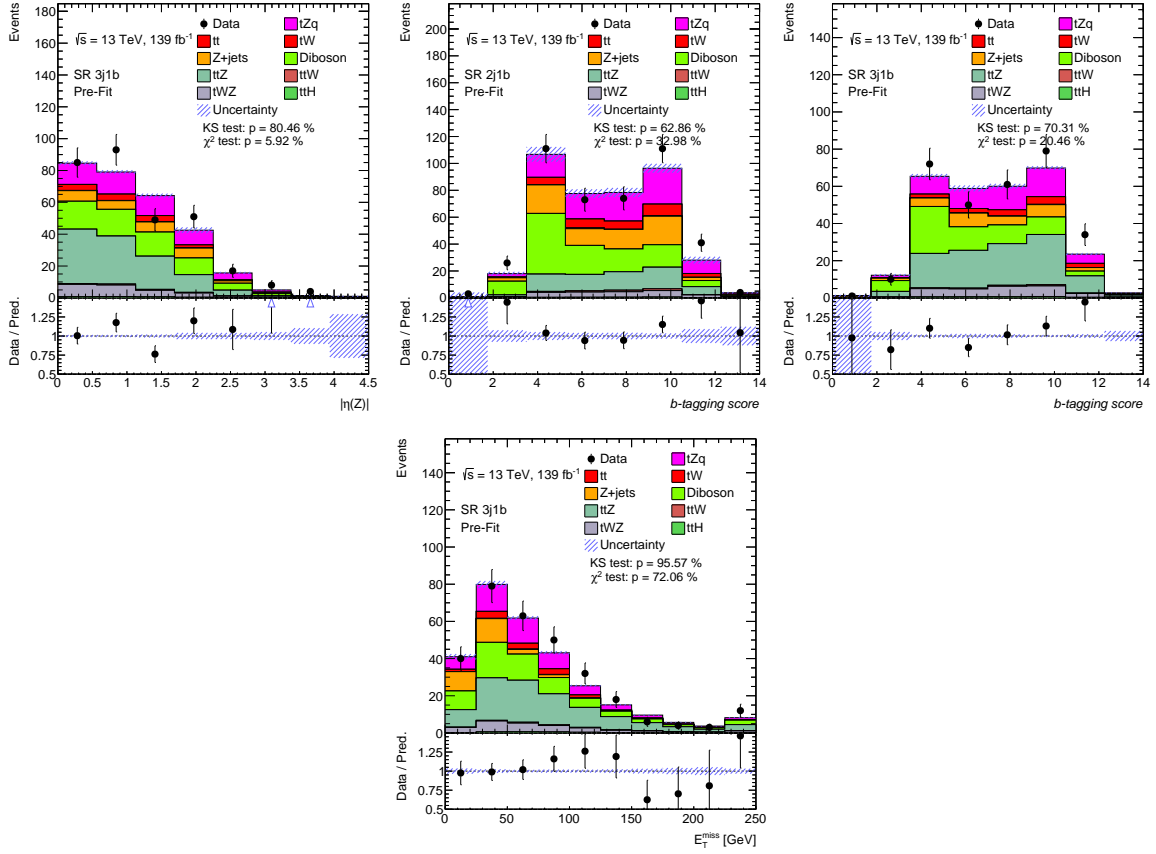
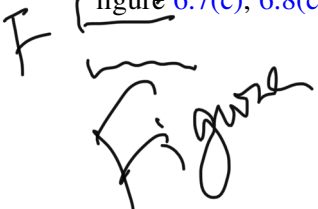


Figure 6.6: Stacked kinematic plots of neural-network training variables of the SR 3j1b, in order of significance. Both signal and backgrounds are normalised to the expected number of events before the fit. The uncertainty band includes statistical uncertainties for signal and backgrounds

6.3.3 NN training in the SRs and $t\bar{t}Z$ CRs

In this section, the results of the NN training is presented. Before the training the MC samples are divided into training and test samples which is also called validation samples. The main idea of splitting the dataset into a training and a validation set is to prevent the model from over-fitting. Training dataset is the set of data that is used to train and make the model learn the hidden features/patterns in the data. In each epoch, the same training data is fed to the neural network repeatedly, and the model continues to learn the features of the data. The validation dataset is the set of data separate from the training set, that is used to validate our model performance during training. The validation process gives information that helps us tune the model's hyperparameters and configurations accordingly. The training results for SR 2j1b, SR 3j1b, CR 3j2b and CR 4j2b are shown in figure 6.7, 6.8, 6.10 and 6.11 respectively.

In supervised learning, a machine learning algorithm builds a model by examining many examples and attempting to find a model that minimizes the loss. Loss is a number indicating how bad was a single example. If the model's prediction is perfect, the loss is zero; otherwise, the loss is greater. figure 6.7(c), 6.8(c), 6.10(a) and 6.11(c) show the loss during training at each epoch. The model



accuracy is shown in figure 6.7(d), 6.8(d), 6.10(b), and 6.11(d) whereas the normalized neural network response are shown in figure 6.7(a), 6.8(a), 6.9(a), and 6.11(a). The output of the signal events accumulate around 1, while the background events accumulate the output around 0. The quality of the training is checked by plotting the receiver operating characteristics (ROC) curve which is shown in figure 6.7(b), 6.8(b), 6.9(b) and 6.11(b) for SR 2j1b, SR 3j1b, CR 3j2b and CR 4j2b respectively. The area under the ROC curve (AUC) which provides an aggregate measure of performance across can be interpreted as the probability that the model ranks a random positive event more highly than a random negative event.

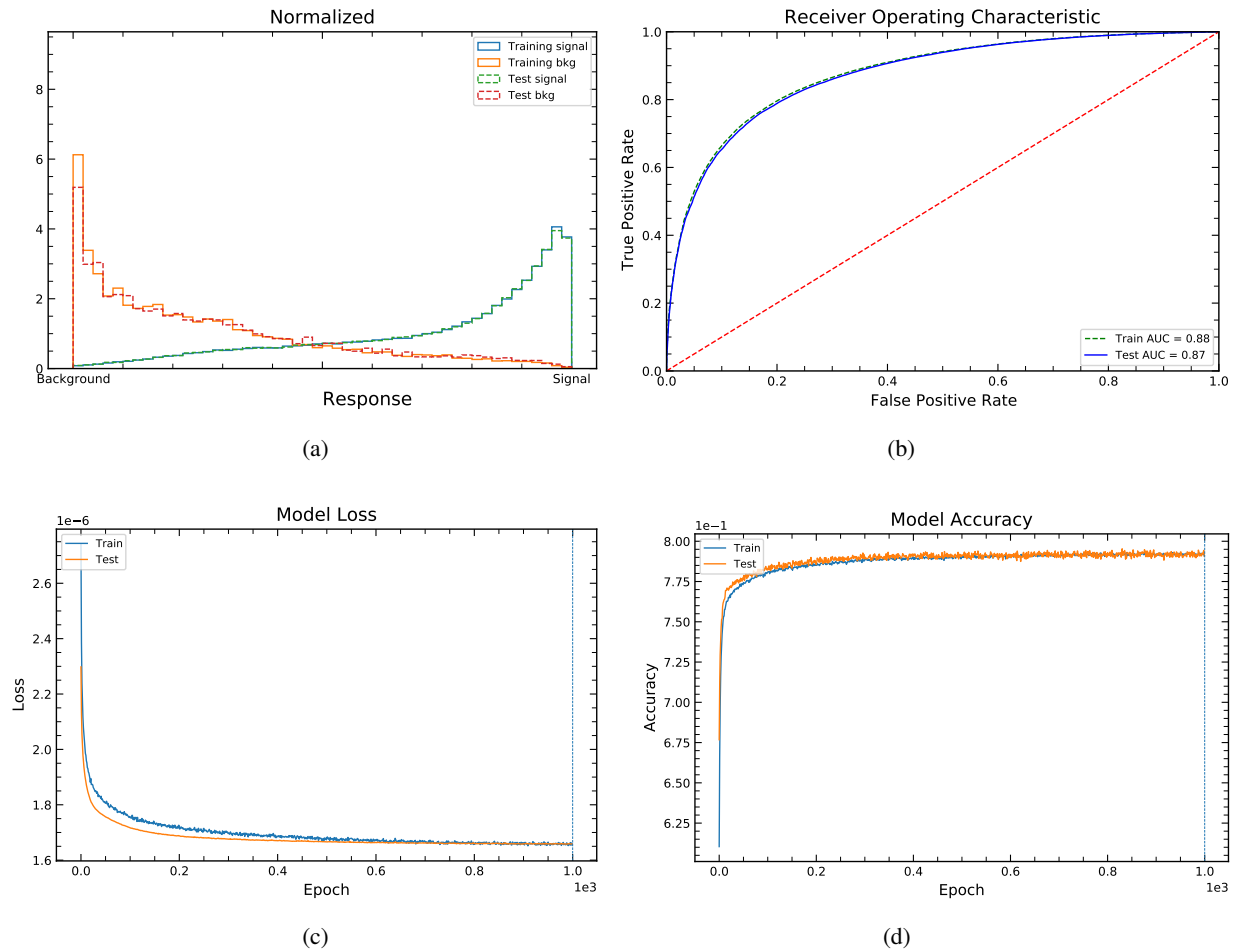


Figure 6.7: Neural Network training output in the SR 2j1b. (a) shows the normalized response of the NN, (b) shows the ROC curve , (c) shows the loss variation during the training and (d) shows the model accuracy for both training and test samples

6.4 Signal extraction - Binned likelihood fit

The likelihood function describes the probability of an observed data as a function of the parameters of the chosen statistical model. In maximum likelihood estimation, the likelihood function is maximized to obtain specific parameter that is most likely to have generated the observed data. In many cases, the

6.4 Signal extraction - Binned likelihood fit

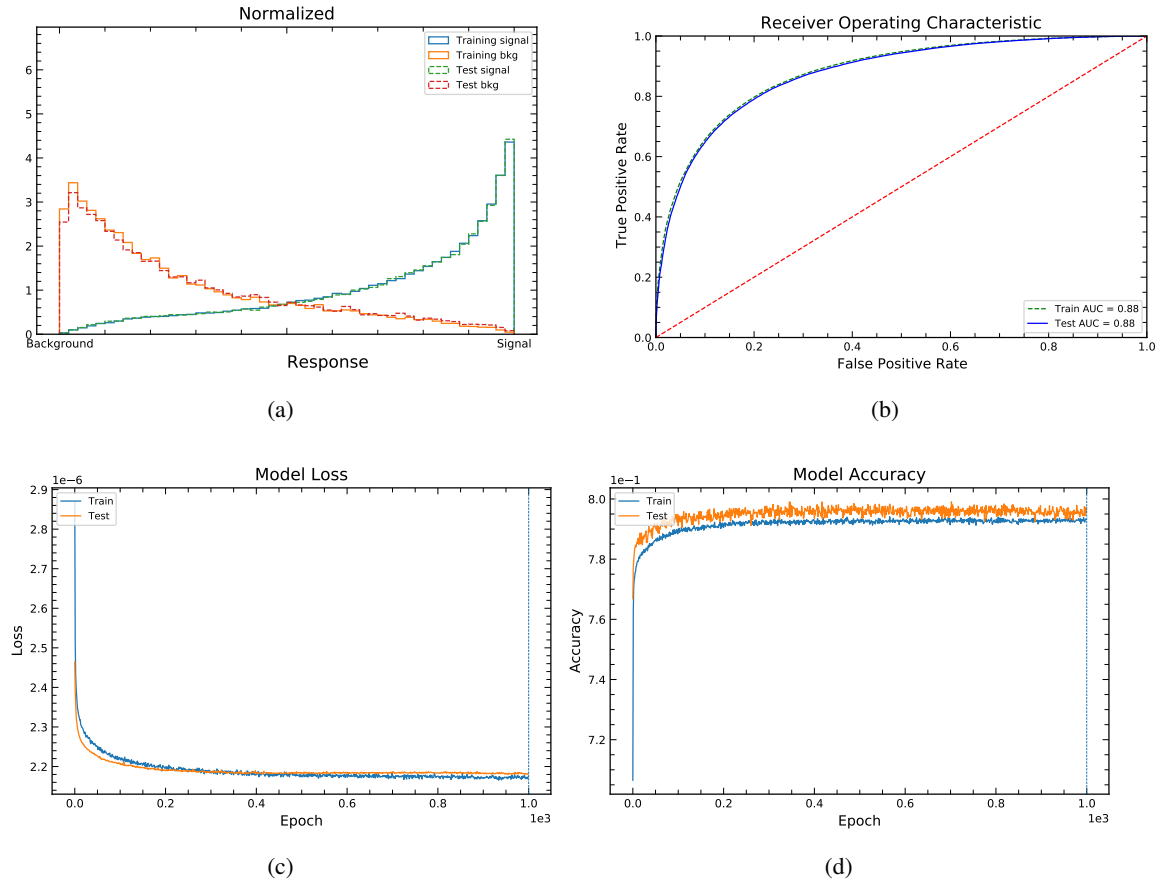


Figure 6.8: Neural Network training output in the SR 3j1b. (a) shows the normalized response of the NN, (b) shows the ROC curve , (c) shows the loss variation during the training and (d) shows the model accuracy for both training and test samples

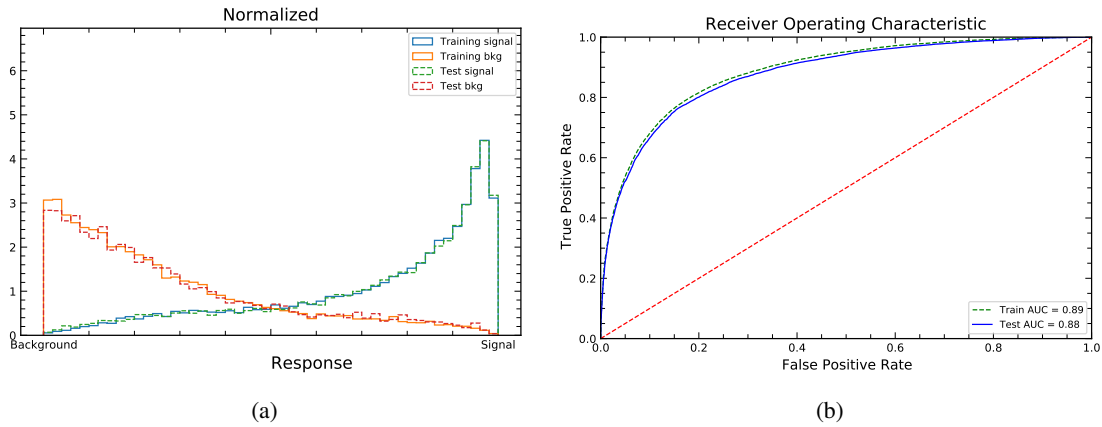


Figure 6.9: Neural Network training output in the CR 3j2b. (a) shows the normalized response of the NN, (b) shows the ROC curve for both training and test samples

Chapter 6 Analysis

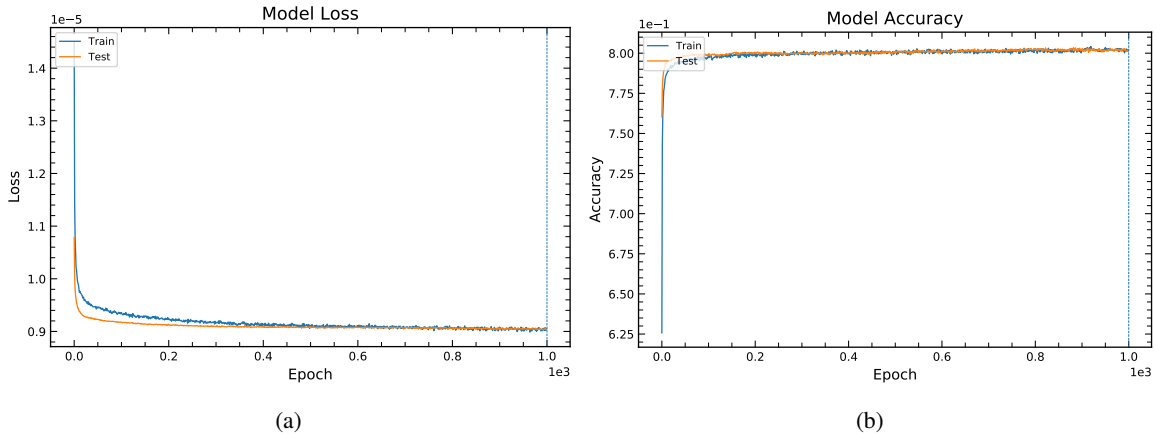


Figure 6.10: Neural Network training output in the CR 3j2b. (a) shows the loss variation during the training and (b) shows the model accuracy for both training and test samples

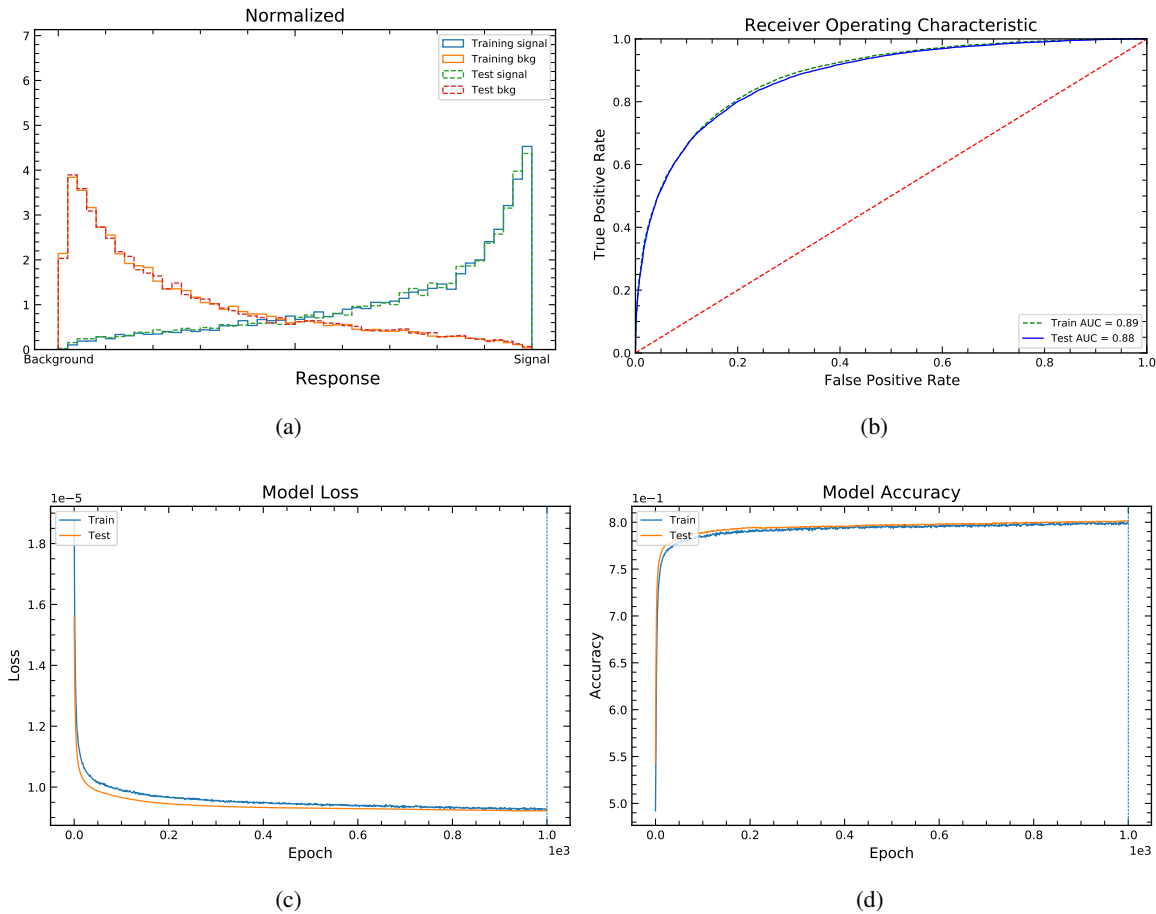


Figure 6.11: Neural Network training output in the CR 4j2b. (a) shows the normalized response of the NN, (b) shows the ROC curve, (c) shows the loss variation during the training and (d) shows the model accuracy for both training and test samples

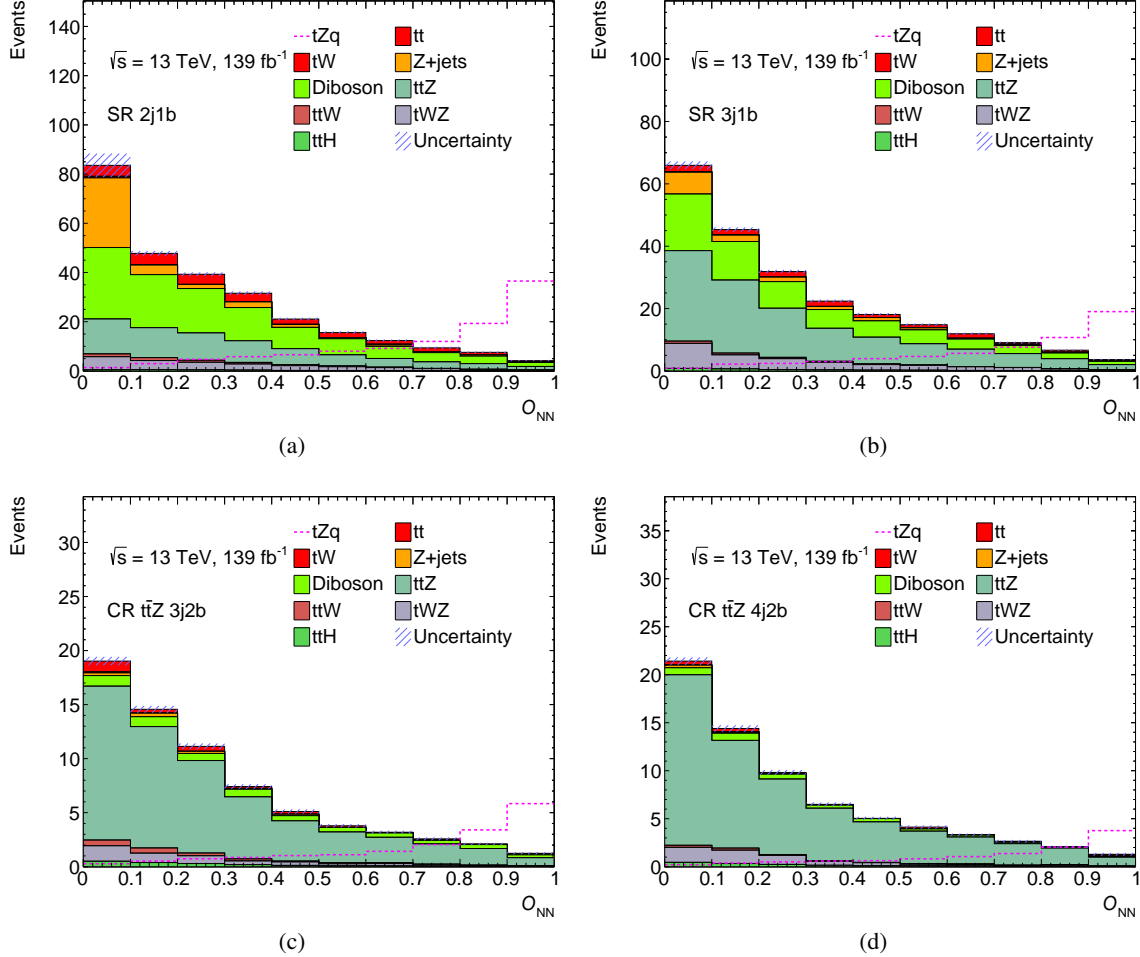


Figure 6.12: Prediction of the Neural Network training in the SR 2j1b, SR 3j1b, CR 3j2b and CR 4j2b. The outputs are normalized w.r.t. their respective cross-section. The signal tZq is overlayed and the backgrounds are stacked.

likelihood is a function of more than one parameter but interest focuses on estimation of only one, or at most a few of them while other being considered as nuisance parameters. Profile likelihood is an approach where a likelihood can be written as a function of only parameter (parameters) of interest. Since in this analysis the selected events are organized in bins, the POI is extracted by performing a binned profile likelihood fit [33]. The likelihood is product of Poisson probability terms for all the bins which can be expressed as:

$$\mathcal{L}(n | \mu, \vec{\theta}) = \prod_{i \in bins} \mathcal{P}(n_i | \mu \cdot S_i(\theta) + B_i(\theta)) \times \prod_{j \in syst} \mathcal{G}(\theta_j^0 | \theta_j, \Delta\theta_j) \quad (6.2)$$

Here, POI is the signal strength μ which is the ratio between the measured tZq cross-section and the SM prediction $\sigma_{tllq} = 102$ fb, n_i is the observed number of events in bin i , while S_i and B_i are the predicted numbers of signal and background events; $\vec{\theta}$ is the set of nuisance parameters introduced

for characterizing the impact of systematic uncertainties into the likelihood function where $\theta = 0$ corresponds to the nominal MC prediction and $\theta = \pm 1$ corresponds to the respective $\pm 1\sigma$ variation and all the nuisance parameters (NPs) are constrained by a Gaussian prior term with $\theta_j^0 = 0$ and $\Delta\theta_j^0 = 1$.

To perform the fit, the TRExFitter software package [34] is used which combines the functionalities of RooFit [35] and RooStats [36]. It allows to define signal and also control regions which can be fitted simultaneously. Furthermore, it provides many features, for example smoothing of histograms, pruning, and symmetrisation of systematic uncertainties

6.4.1 Fitted regions

The SRs included in the fit are designed to maximize sensitivity to the POI, and the CRs are designed to maximally constrain nuisance parameters so as to have maximum information extraction of the POI. The regions and the corresponding distributions that are fitted are summarized in table ?? For the SRs and $t\bar{t}Z$ CRs, the output of O_{NN} distribution is used in the fit. For the diboson CRs, the transverse mass of W boson $m_T(W)$ distribution is used. The $m_T(W)$ distribution also contains Z+jets in the first bins. For the $t\bar{t}$ CRs a single bin m_{bj_f} distribution. Due to relatively low statistics, the used variable is irrelevant.

Region	Distribution	Additional info
SR 2j1b	O_{NN}	–
SR 3j1b	O_{NN}	–
CR diboson 2j0b	$m_T(\ell, E_T^{miss})$	–
CR diboson 3j0b	$m_T(\ell, E_T^{miss})$	–
CR $t\bar{t}$ 2j1b	m_{bj_f}	Single bin
CR $t\bar{t}$ 3j1b	m_{bj_f}	Single bin
CR $t\bar{t}Z$ 3j2b	O_{NN}	–
CR $t\bar{t}Z$ 4j2b	O_{NN}	–

Table 6.2: Overview of the regions included in the fit

6.4.2 Binning optimization

To find the best binning for the distributions in each fitted regions, the TransfoD method in the AutoBin function in TRExFitter is used. There are two parameters in the function ns and nb. When ns = 0 (nb = 0), background (signal) distribution is flat, namely, each bin contains the same number of events. In this optimization, asimov data is used and all systematic are included in the significance calculation (based on TRExFitter) as used in the final fit. The significance for different ns, nb combinations in each fitted regions is given in table 4.2. Finally to avoid any empty bins, only 10 bins are used in the SRs.

6.5 Systematics uncertainties

Systematic uncertainties are the possible unknown variations in measurements that are not directly caused by data statistics. Many sources of systematic uncertainties are considered in the extraction of the tZq total cross-section. Each source of systematic uncertainty effects the predicted signal and background modeling. The impact of each uncertainty is propagated to each histogram bins yield and is constrained by individual Gaussian nuisance parameter (NP) in the maximum likelihood fit as shown in eqn. 6.2.

6.5.1 Sources of systematics uncertainties

The systematic uncertainties can arise due to imprecise knowledge of the detector acceptance, calibration and resolutions, choice of input parameters in the MC simulations, imprecise measurement of the luminosity or uncertainties on the method used for background. The sources of systematic uncertainties that are used in the fit are introduced below.

6.5.2 Experimental uncertainties

Luminosity

The uncertainty in the combined 2015–2018 integrated luminosity is 1.7 %. The values is derived with methods described in Ref. [37] and by using the LUCID-2 detector for the luminosity measurements [38].

Pile-up reweighting

As described in Section 4.2, all MC samples are reweighted in order to match the level of pile-up observed in data [39]. Uncertainties related to the pile-up scale factors have to be propagated into the fit. An up and a down variation are provided.

Lepton reconstruction, identification, isolation and trigger

Reconstruction, identification, isolation and trigger performance for electrons and muons differ between data and MC. To correct these differences, scale factors related to the mentioned procedures are applied. This is done by selecting events that have a clear leptonic signature, such as $Z \rightarrow \mu^+ \mu^-$ and $Z \rightarrow e^+ e^-$ events. The uncertainties are evaluated by varying the lepton and signal selection and from the uncertainties in the background evaluations [40, 41]

Jet vertex tagger efficiency

For the cross-section measurement, it is necessary to distinguish between pile-up and jets from the hard scattering process. Therefore, the efficiency of the jet vertex tagger (JVT) needs to be precisely known. An uncertainty associated to the JVT scaling factor is assigned, which is estimated by taking into account differences observed when using different MC generators in $Z+jets$ events, statistical uncertainty and additional uncertainty due to residual pile-up contamination [42].

Flavour tagging

A flavour-dependant efficiencies and their uncertainties are evaluated from the data [43]. Efficiencies of heavy flavour jets (b and c jets) need to be corrected by p_T dependant scale factors in simulations. The uncertainty on the scale factors are de-correlated result in nine eigen-vectors (EV) for b-tag efficiencies, four EV of c-tag efficiencies and six EV for light-flavour efficiencies.

6.5.3 Theoretical uncertainties

MC background normalisation

Normalization uncertainties are assigned to all MC background distributions in order to take into account the theoretical uncertainties on the predicted cross-sections as well as the uncertainties on the acceptances. For the single top-quark backgrounds, acceptance effects are already taken into account in the modelling uncertainties. Therefore, the total uncertainties (PDF + α_s , and QCD scale uncertainties) on the predicted cross-section is used. The expected overall rate uncertainty for the background process are shown in Table 6.3 from Ref.[44].

Process	Uncertainty
$t\bar{t} + tW$	7%
Z+jets	15%
Diboson	30%
$t\bar{t}Z + tWZ$	12%
$t\bar{t}H + t\bar{t}W$	15%

Table 6.3: Overview of normalisation uncertainties for the background processes.

Signal PDF and radiation

The systematic effects due to uncertainties in the parton distribution function, and in the renormalization and factorization scales and in the amount of additional radiation is signal modeling uncertainties. The uncertainty in the renormalization, factorization scales and in the amount of additional radiation are referred to as "tZq QCD radiation". The tZq PDF uncertainty is 2.2%, and the tZq QCD radiation is 10.8% (Ref. [44]). The details on tZq signal modelling uncertainty are given in Ref. [44].

6.5.4 Symmetrizing, smoothing and pruning

To reduce the complexity and increase the speed and stability of the fit, pruning, symmetrizing and smoothing procedure is applied within TRExFitter framework. Systematic uncertainties which have an effect smaller than 0.05% on the normalization are only considered for the shape effect. Uncertainties with an effect smaller than 0.1% on the shape are only considered for the normalisation effect. MC statistical uncertainties are also removed from the fit if the uncertainty in the specific bin is lower than 0.1%.

Results

In this chapter, the results of the fit is presented. In order to assess the results of the fit, comparisons between the pre-fit and post-fit plots, event yields and uncertainties are studied.

Section 7.1 summarises the expected fit results that are obtained by performing the binned likelihood fit on the asimov data. In section 7.2, the results of the fit performed on the data is presented. Section 7.3 presents a discussion of the gives, including a brief comparison with the recent tZq cross-section measurement published by both ATLAS and CMS experiment.

7.1 Expected fit results

The expected fit results are the one that are obtained by performing the so-called Asimov fit. Asimov fit is a test fit performed on the pseudo data, where the combination of predicted background and signal assuming a signal strength of $\mu = 1$, is used. The nominal distributions are used to create this dataset i.e. all the NPs are set to zero in the Asimov fit and exactly matches signal plus background hypothesis as shown in figure 7.1.

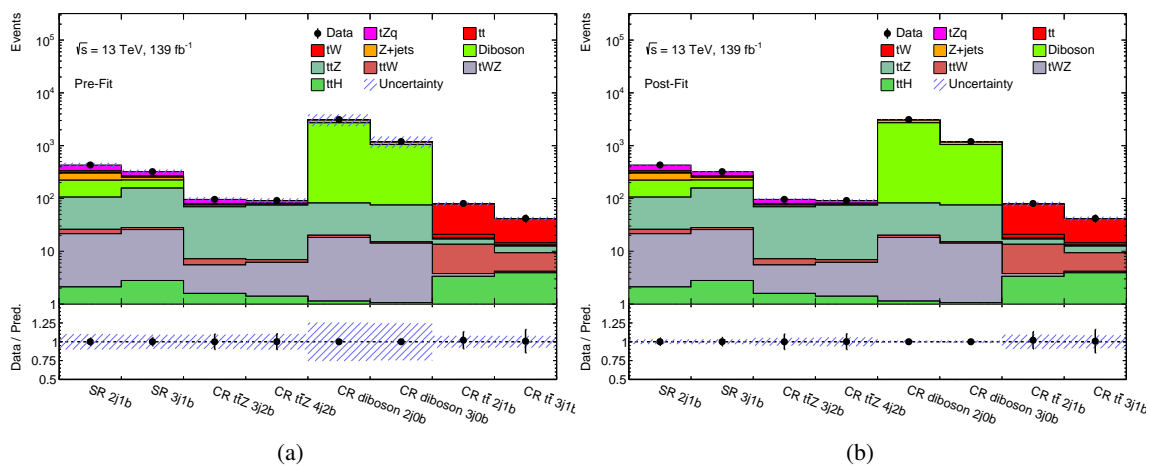


Figure 7.1: Summary of the plots of events in the signal and control regions during the Asimov fit. The implemented Asimov fit is a hybrid one. (a) Pre-fit (b) Post-fit

The post-fit values (pulls) of all NPs have to be close to zero while the post-fit uncertainties can be smaller than their pre-fit uncertainties due to constrain on uncertainties. The result is $\mu = 1$, which corresponds to an expected uncertainty of 20%. The total uncertainties include both the statistical and the systematic uncertainties. The post-fit values of all the NPs are shown in figure 7.2(a) and all are centered around zero. The pull of the gammas is shown in figure 7.2(b).

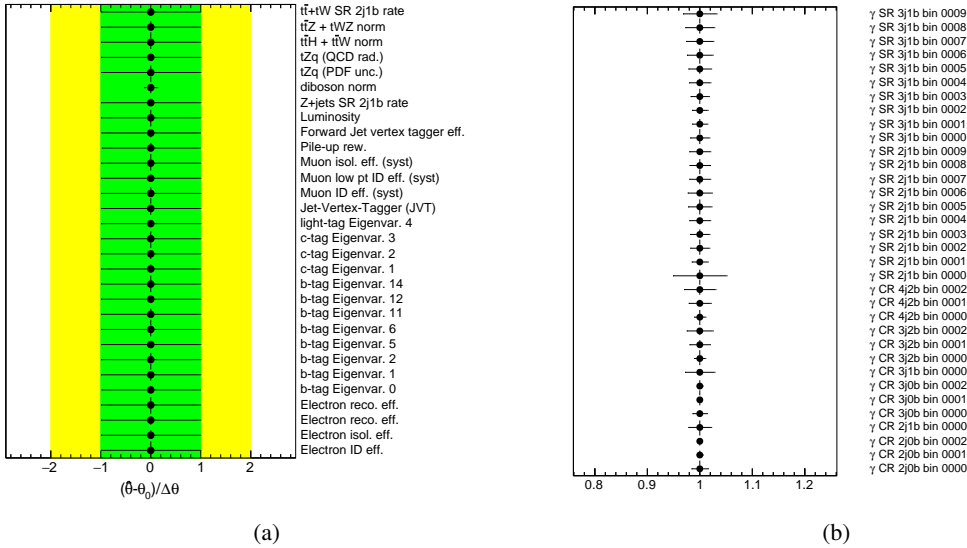


Figure 7.2: (a) Pull distributions of nuisance parameters associated to systematic uncertainties using the blinded dataset. Only nuisance parameters substantial effect are shown. (b) Pull distributions of bin gamma parameters in the blinded fit.

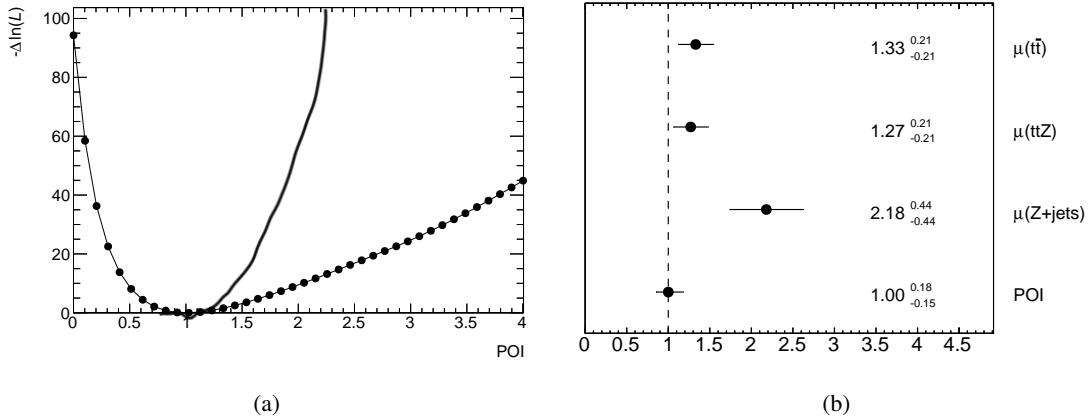


Figure 7.3: (a) The likelihood scan of the signal strength (μ) or parameter of interest (POI) and (b) NormFactors of the free floating parameters used in the fit.

In order to check the stability, the likelihood scan of the signal strength (μ) is performed. The resulting (minimised) negative log-likelihood plot is shown in figure 7.3(a). The curve has a very

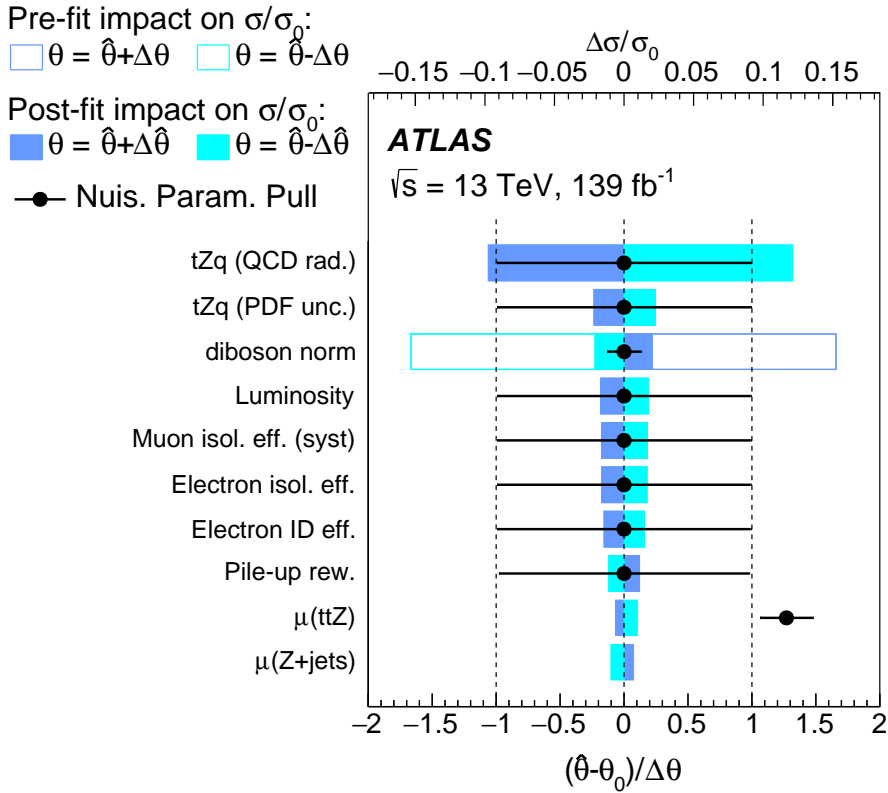


Figure 7.4: The ranking plot showing the impact of each NP on μ in the Asimov fit. There, the empty/full boxes show the pre-/post-fit impacts while the black dots/lines represent the post-fit values/uncertainties of all NPs. Only the 10 NPs with the highest post-fit impacts are displayed.

smooth and parabolic shape which says that the fit configuration is stable and results are reliable. The norm factors of the Asimov fit is shown in figure 7.3(b). To get an idea of which NPs have the largest impact on the fitted signal strength, their ranking is investigated, which is shown in figure 7.4. It can be concluded that the uncertainty on the signal strength is dominated by the tZq QCD radiation uncertainties.

7.2 Observed fit results

The fit configuration that was tested on pseudo data in the previous section, is used to fit the observed full Run II data in order to extract the signal strength and thereby the cross-section. The pre-fit and post-fit of the fitted distributions in the signal and control regions are shown in fig. The event yields of the pre-fit and post-fit are shown in Table 7.1. Comparing to the post-fit distributions in fig. 7.5 to the pre-fit distributions in figure 7.5 and 7.6, one can observe that the agreement with data is significantly improved. Also, the total uncertainty is significantly reduced after fit. This can be due to constrain on NPs and anti-correlations between NPs also reduces the uncertainties.

The pull of all NPs obtained when fitting signal regions and control regions simultaneously to the data are shown in figure 7.7(a). It shows that only few pulls are away from zero but are still within

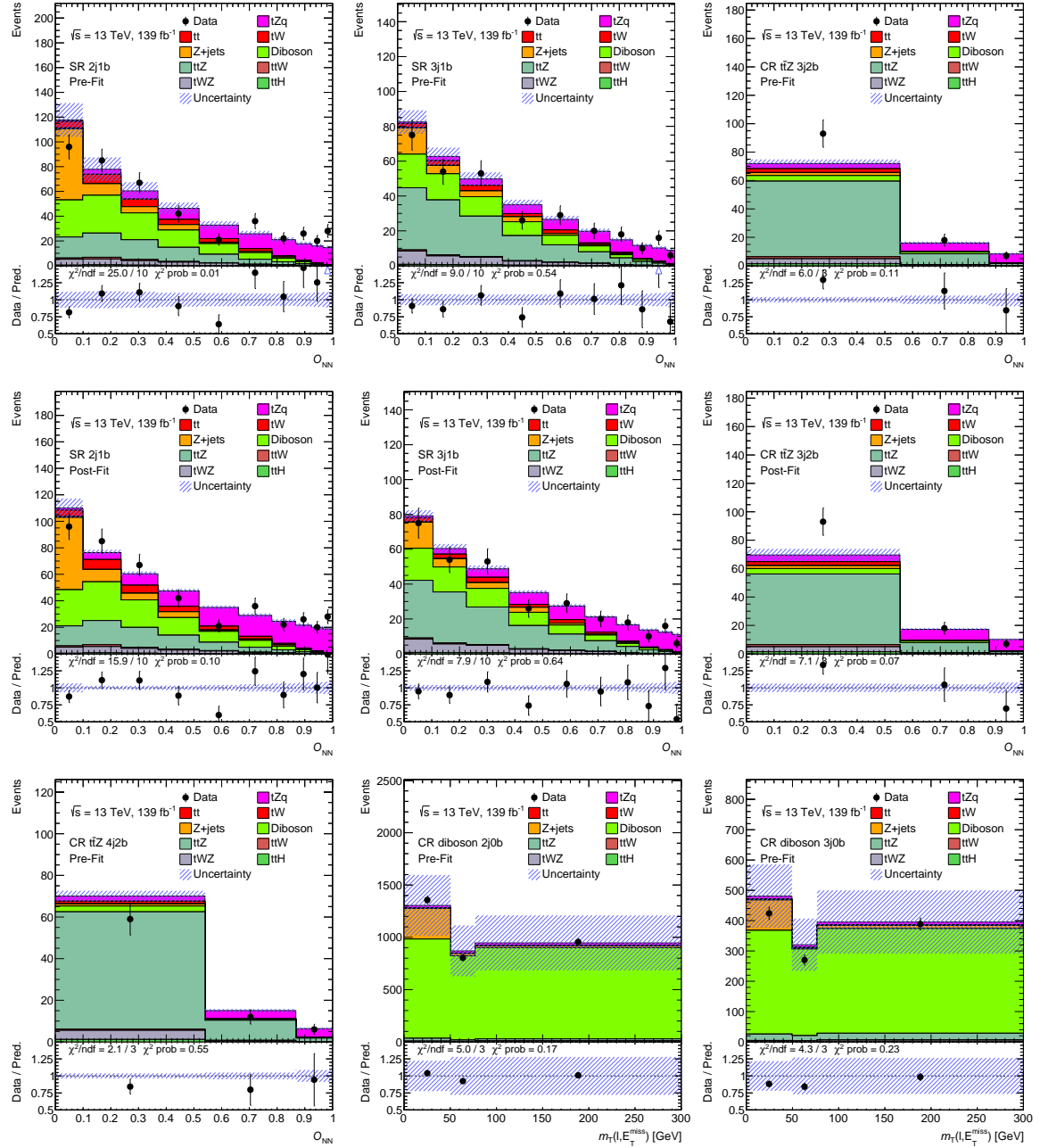


Figure 7.5: Pre-fit (left) and post-fit (right) distributions in the signal regions and control regions described in the table 6.2. The black points show the unbinned dataset. The error band includes the statistical and systematic uncertainties.

the respective $\pm 1\sigma$ bands. The NPs with largest pull are related to (names). The pulls are further studied to see if they are able to compensate the difference between the prediction (signal+background) and data. Therefore, histograms showing the effects of three uncertainties on the total prediction are investigated in figure 7.11 and 7.12. Finally, the measured signal strength in the observed data is

7.2 Observed fit results

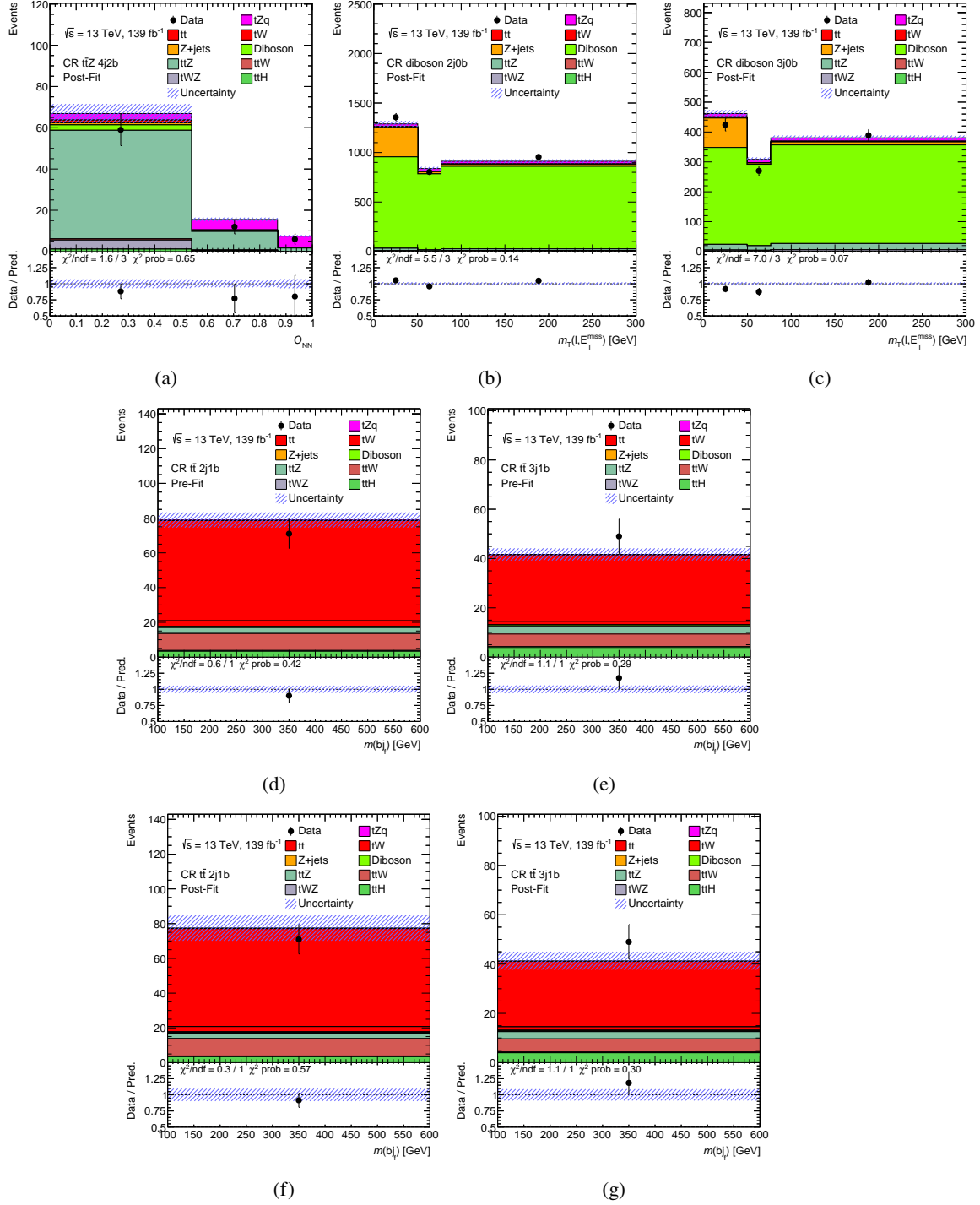


Figure 7.6: Pre-fit (left) and post-fit (right) distributions in the signal regions and control regions described in the table 6.2. The black points show the unblinded dataset. The error band includes the statistical and systematic uncertainties.

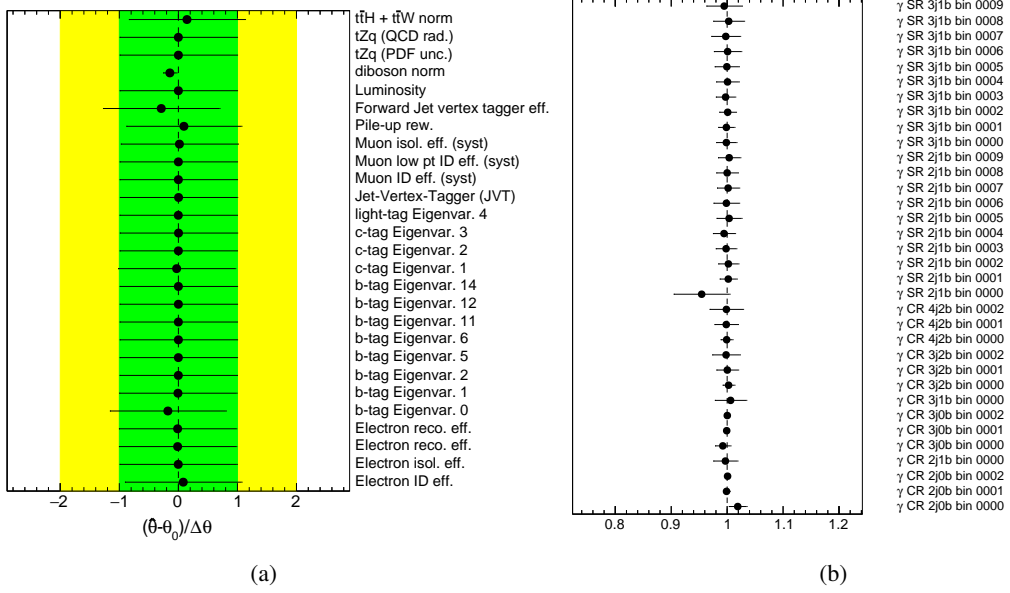


Figure 7.7: (a) Pull distributions of nuisance parameters associated to systematic uncertainties using the full unblinded dataset. Only nuisance parameters substantial effect are shown. (b) Pull distributions of bin gamma parameters in the unblinded fit.

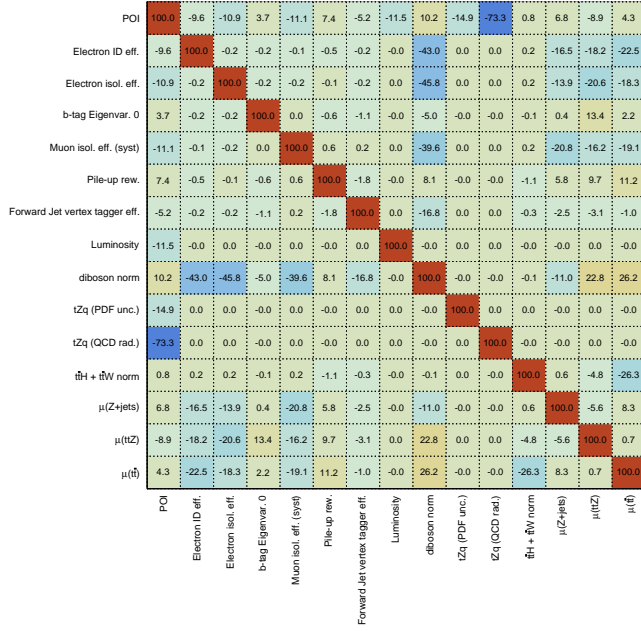


Figure 7.8: Correlation matrix of the parameters included in the likelihood fit for the data.

7.2 Observed fit results

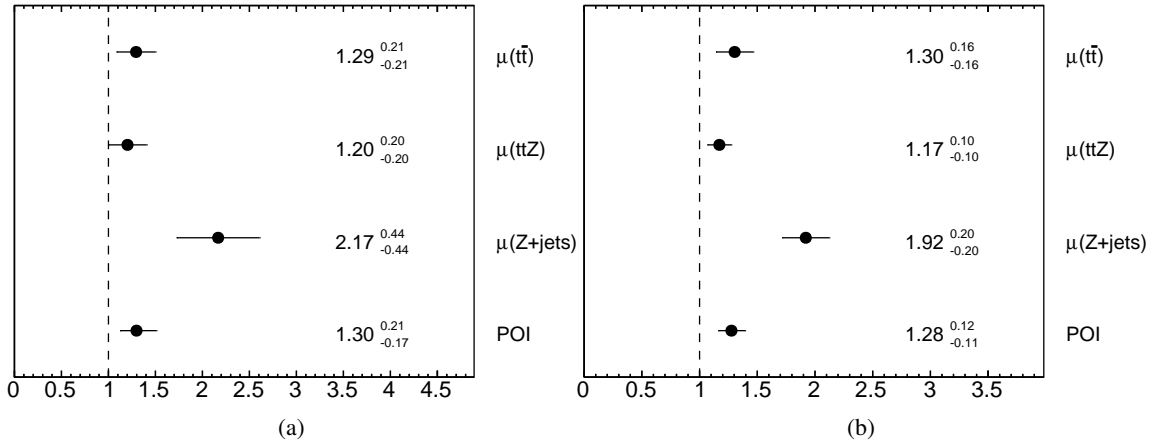


Figure 7.9: NormFactors of the free floating parameters during the binned profile likelihood fit in the signal regions and control regions for the data.(a) Syst + Stat fit (b) Statonly fit

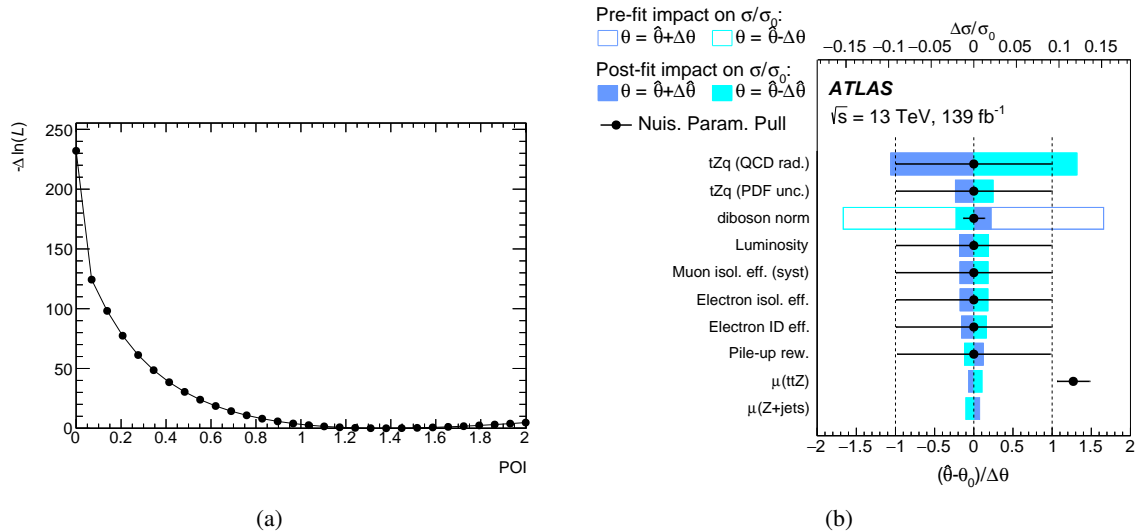


Figure 7.10: (a) The likelihood scan of the signal strength (μ) or parameter of interest (POI) and (b) The ranking plot showing the impact of each NP on μ in the unblinded fit. There, the empty/full boxes show the pre-/post-fit impacts while the black dots/lines represent the post-fit values/uncertainties of all NPs. Only the 10 NPs with the highest post-fit impacts are displayed.

$\mu = 1.30$ with a total uncertainty of 4.3%. Here, the total uncertainty is quoted which is directly quoted from the profile-likelihood fit. Multiplying the signal strength with the SM prediction $\sigma_{t\bar{t}lq}^{SM} = 102$ fb, the measured $t\bar{t}lq$ cross-section is determined to be 132 ± 12 (stat) ± 17 (syst) fb. The statistical uncertainty is obtained by performing statonly fit as shown in figure 7.9(b). The systematic uncertainty is then obtained by subtracting the statistical uncertainty in quadrature form from the total uncertainty. The curve obtained after performing the negative loglikelihood scan of the signal strength (POI) is shown in figure 7.10(a). As in the asimov fit, the curve is parabolic and smooth which shows that the fit is stable and results and uncertainties are reliable. The ranking of NPs is shown in figure 7.10(b). which is very similar comared to the ranking in the Asimov fit shown in fig. The relative order slightly

Chapter 7 Results

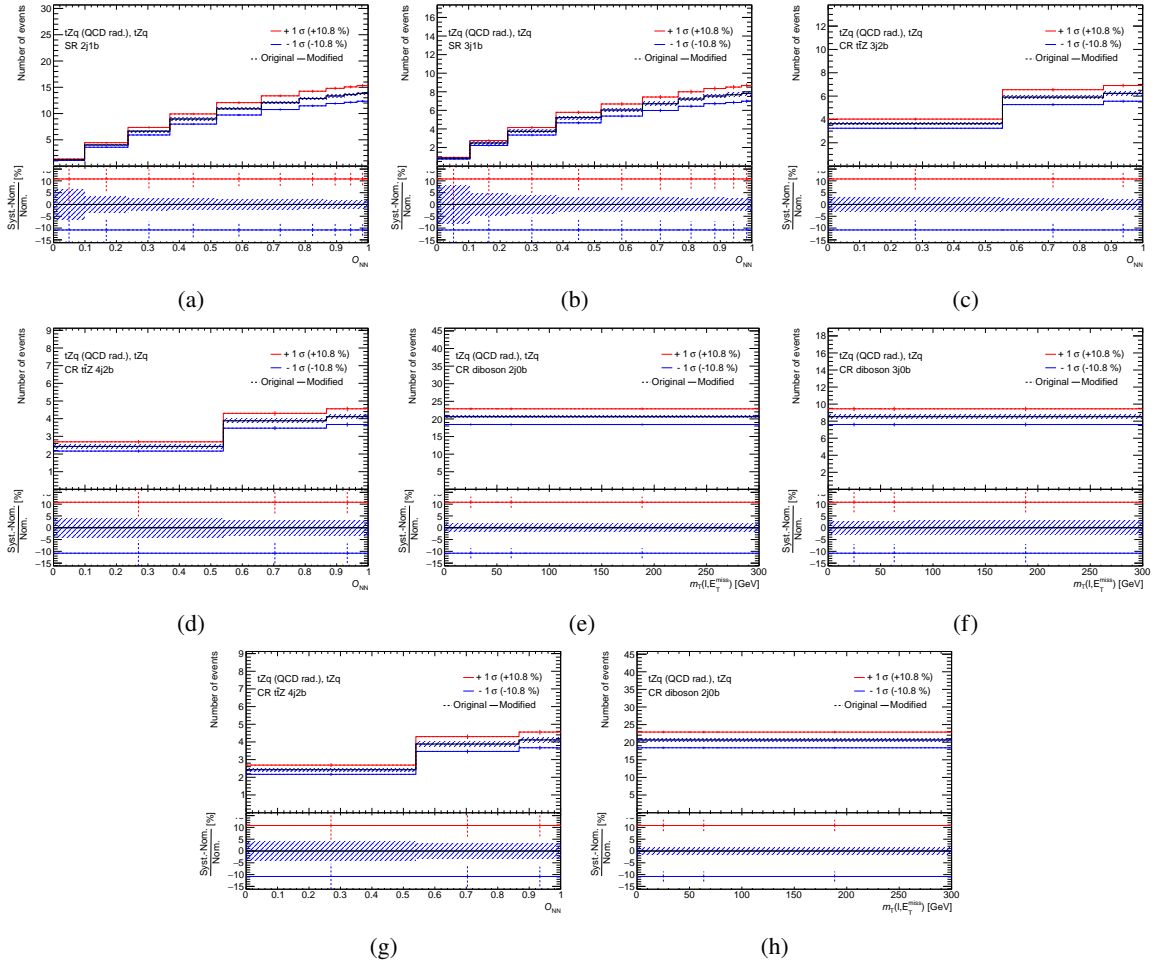
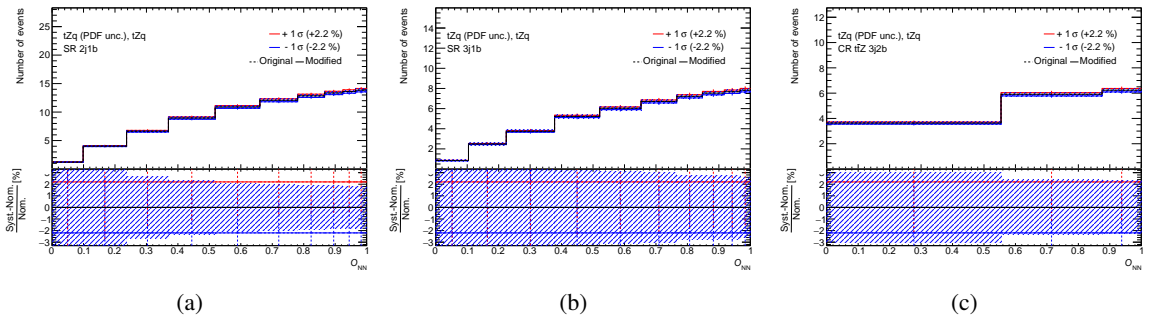


Figure 7.11: The effects of the tZq QCD rad. on the total prediction in the signal and control regions. Here, lines coloured in red/blue present the $\pm 1\sigma$ effect. The dotted/solid lines show the effect before/after smoothing, symmetrisation, and the removal of the normalisation effect (only done for shape uncertainties). The hashed bands represent the MC statistical uncertainties.



differs because the post-fit values are different which in principle can change the impact.

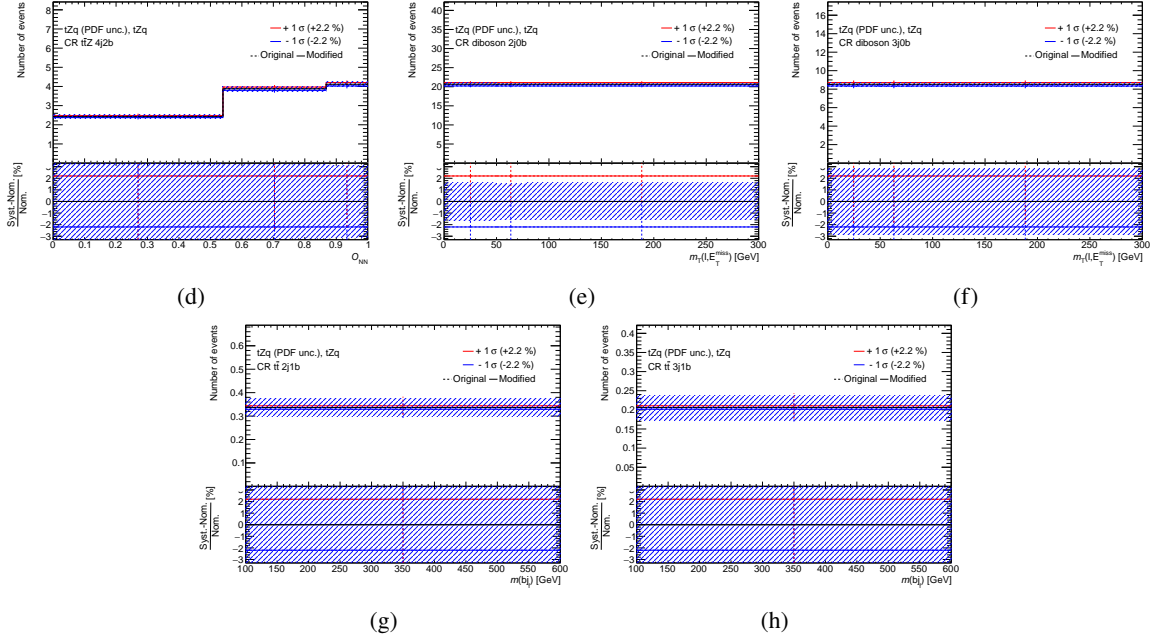


Figure 7.12: The effects of the tZq PDF uncert. on the total prediction in the signal and control regions. Here, lines coloured in red/blue present the $\pm 1\sigma$ effect. The dotted/solid lines show the effect before/after smoothing, symmetrisation, and the removal of the normalisation effect (only done for shape uncertainties). The hashed bands represent the MC statistical uncertainties.

7.3 Discussion of the results

The measured value of the signal strength is $1.30 \pm 0.12 \pm 0.17$. The measurement is dominated by the systematic uncertainties. A comparison between several top quark production cross-section measurements performed in ATLAS is shown in figure 7.13. The rare tZq process because of its low cross-section was only measured using Run II datasets at $\sqrt{s} = 13$ TeV. The measurement is performed by both ATLAS and CMS and to compare the results, a summary of both ATLAS and CMS analysis is given in table 7.1.

	ATLAS (tllq)	CMS (tllq)
μ		
$\sigma_{SM}(tllq)$	102 fb	
$\sigma(tllq)$	fb	

Table 7.1: Overview of the final results for the ATLAS (tllq) cross-section and CMS (tllq) measurements.

The used strategy and strategies for the ATLAS and CMS measurements are similar. For separating signal and backgrounds, python based (Tensorflow, NN) MVA technique is used whereas NeuroBayes (NN) for ATLAS and boosted decision trees for CMS were used. Signal extraction is done using a binned likelihood fit. The measured cross-section is higher than the recent measurements performed by ATLAS and CMS collaborations. The discrepancy in measurement can be due different signal

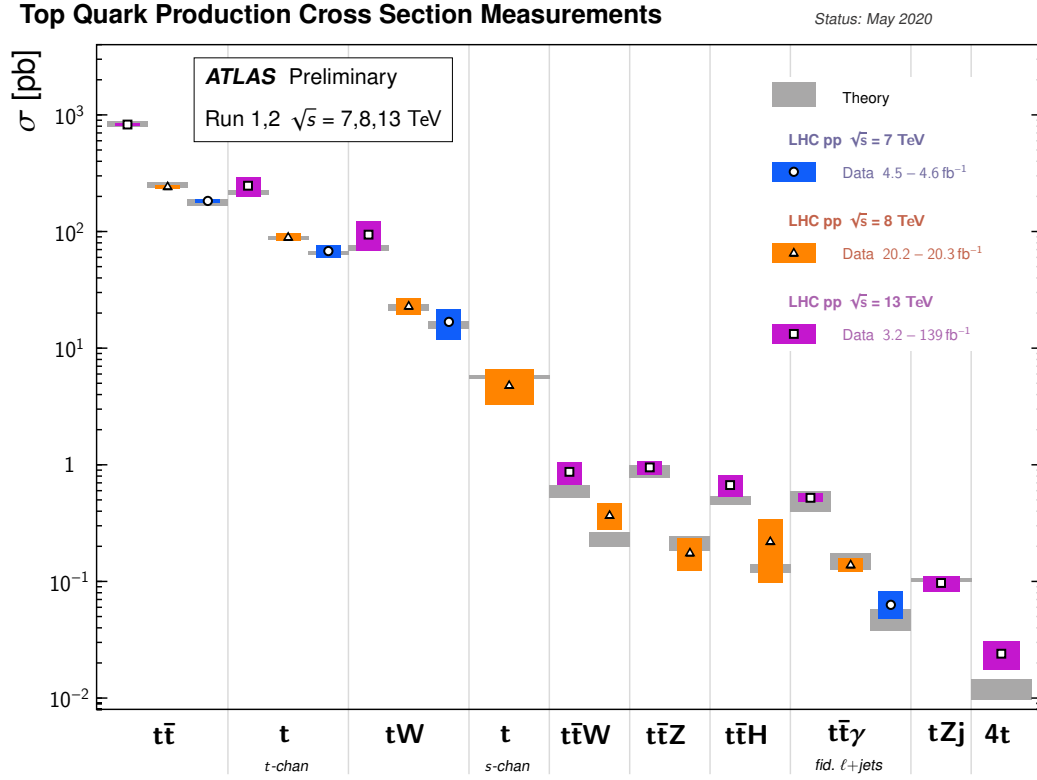


Figure 7.13: Summary of several SM total production cross-section measurements at different centre-of-mass energies [45]

and background event yields or the different treatment of systematic uncertainties. The $t\bar{Z}q$ QCD radiation and PDF uncertainties have largest impact on the signal strength while uncertainties due to luminosity have largest impact on the signal strength in ATLAS analysis[31].

CHAPTER 8

Conclusion

This thesis describes the analysis and measurement of a rare Standard Model process, the associated production of a single top-quark and a Z boson using full Run II dataset (2015-2018) which corresponds to an integrated luminosity of 139 fb^{-1} . The measurement is performed in the tri-lepton channel. This channel offers maximum reach in spite of the suppressed branching ratios as the presence of the three charged leptons in the final state significantly reduces the background. A python based (tensorflow) neural network algorithm is trained in order to separate the signal and background distributions. A simultaneous binned maximum-likelihood fit of the signal regions and control regions is performed and from the fit cross-section is extracted. The extracted cross-section of ~~all~~ is $\sigma(pp \rightarrow tZq \rightarrow Wbl^+l^-q) = 132 \pm 12 \text{ (stat)} \pm 17 \text{ (syst)} \text{ fb}$ with the SM prediction of 102 fb under the assumption of a top-quark mass of $m_t = 172.5 \text{ GeV}$.



Bibliography

- [1] V. M. Abazov et al., *Observation of Single Top-Quark Production*, Phys. Rev. Lett. **103** (9 2009) 092001, URL: <https://link.aps.org/doi/10.1103/PhysRevLett.103.092001>.
- [2] T. Aaltonen et al., *Observation of Electroweak Single Top-Quark Production*, Phys. Rev. Lett. **103** (9 2009) 092002, URL: <https://link.aps.org/doi/10.1103/PhysRevLett.103.092002>.
- [3] G. Aad et al., *Measurement of the t -channel single top-quark production cross section in pp collisions at $\sqrt{s} = 7$ TeV with the ATLAS detector*, Phys. Lett. B **717** (2012) 330, arXiv: [1205.3130 \[hep-ex\]](https://arxiv.org/abs/1205.3130).
- [4] S. Chatrchyan et al., *Measurement of the t -Channel Single Top Quark Production Cross Section in pp Collisions at $\sqrt{s} = 7$ TeV*, Phys. Rev. Lett. **107** (9 2011) 091802, URL: <https://link.aps.org/doi/10.1103/PhysRevLett.107.091802>.
- [5] M. E. Peskin and D. V. Schroeder, *An Introduction to quantum field theory*, Addison-Wesley, 1995, ISBN: 978-0-201-50397-5.
- [6] Carsten Burgard, David Galbraith, *A standard diagram of the current standard model of physics*, (2012), URL: <http://davidgalbraith.org/portfolio/ux-standard-model-of-the-standard-model/>.
- [7] M. Bariotti et al., *Present knowledge of the Cabibbo-Kobayashi-Maskawa matrix*, Riv. Nuovo Cim. **23N3** (2000) 1, arXiv: [hep-ph/0001293](https://arxiv.org/abs/hep-ph/0001293).
- [8] J. H. Christenson et al., *Evidence for the 2π Decay of the K_2^0 Meson*, Phys. Rev. Lett. **13** (4 1964) 138, URL: <https://link.aps.org/doi/10.1103/PhysRevLett.13.138>.
- [9] M. Kobayashi and T. Maskawa, *CP -violation in the renormalizable theory of weak interaction*, Progress of theoretical physics **49** (1973) 652.
- [10] S. W. Herb et al., *Observation of a Dimuon Resonance at 9.5 GeV in 400-GeV Proton-Nucleus Collisions*, Phys. Rev. Lett. **39** (5 1977) 252, URL: <https://link.aps.org/doi/10.1103/PhysRevLett.39.252>.
- [11] F. Abe et al., *Observation of Top Quark Production in $\bar{p}p$ Collisions with the Collider Detector at Fermilab*, Phys. Rev. Lett. **74** (14 1995) 2626, URL: <https://link.aps.org/doi/10.1103/PhysRevLett.74.2626>.

Bibliography

- [12] S. Abachi et al., *Observation of the Top Quark*, Phys. Rev. Lett. **74** (14 1995) 2632, URL: <https://link.aps.org/doi/10.1103/PhysRevLett.74.2632>.
- [13] C. Patrignani et al., *Review of Particle Physics*, Chin. Phys. C **40** (2016) 100001.
- [14] R. Schwienhorst, *Top cross-sections and single top*, International Journal of Modern Physics: Conference Series **31** (2014) 1460277, ISSN: 2010-1945, URL: <http://dx.doi.org/10.1142/S2010194514602774>.
- [15] Standard Model Results, *Summary plots from the ATLAS Standard Model physics group*, (), URL: <https://atlas.web.cern.ch/Atlas/GROUPS/PHYSICS/PUBNOTES/ATL-PHYS-PUB-2020-012/>.
- [16] J. Haffner, *The CERN accelerator complex. Complexe des accélérateurs du CERN*, (2013), General Photo, URL: <https://cds.cern.ch/record/1621894>.
- [17] J. Pequenao, “Computer generated image of the whole ATLAS detector”, 2008, URL: <https://cds.cern.ch/record/1095924>.
- [18] J. Pequenao and P. Schaffner, “How ATLAS detects particles: diagram of particle paths in the detector”, 2013, URL: <https://cds.cern.ch/record/1505342>.
- [19] J. Pequenao, “Computer generated image of the ATLAS inner detector”, 2008, URL: <https://cds.cern.ch/record/1095926>.
- [20] J. Pequenao, “Computer Generated image of the ATLAS calorimeter”, 2008, URL: <https://cds.cern.ch/record/1095927>.
- [21] *Luminosity determination for low-pileup datasets at $\sqrt{s} = 5$ and 13 TeV using the ATLAS detector at the LHC*, tech. rep., CERN, 2020, URL: <http://cds.cern.ch/record/2725195>.
- [22] A. Buckley et al., *Monte Carlo event generators for high energy particle physics event simulation*, 2019, arXiv: [1902.01674 \[hep-ph\]](https://arxiv.org/abs/1902.01674).
- [23] A. Collaboration, *Athena*, version 22.0.1, 2019, URL: <https://doi.org/10.5281/zenodo.2641997>.
- [24] S. Agostinelli et al., *GEANT4—a simulation toolkit*, Nucl. Instrum. Meth. A **506** (2003) 250.
- [25] J. Alwall et al., *The automated computation of tree-level and next-to-leading order differential cross sections, and their matching to parton shower simulations*, Journal of High Energy Physics **2014** (2014), ISSN: 1029-8479, URL: [http://dx.doi.org/10.1007/JHEP07\(2014\)079](http://dx.doi.org/10.1007/JHEP07(2014)079).
- [26] T. Gleisberg et al., *SHERPA 1. , a proof-of-concept version*, Journal of High Energy Physics **2004** (2004) 056, ISSN: 1029-8479, URL: <http://dx.doi.org/10.1088/1126-6708/2004/02/056>.
- [27] T. Gleisberg et al., *Event generation with SHERPA 1.1*, Journal of High Energy Physics **2009** (2009) 007, ISSN: 1029-8479, URL: <http://dx.doi.org/10.1088/1126-6708/2009/02/007>.

-
- [28] C. Oleari, *The POWHEG-BOX*, *Nucl. Phys. B Proc. Suppl.* **205-206** (2010) 36, ed. by J. Blümlein, S.-O. Moch and T. Riemann, arXiv: [1007.3893 \[hep-ph\]](https://arxiv.org/abs/1007.3893).
 - [29] T. Sjöstrand, S. Mrenna and P. Skands, *PYTHIA 6.4 physics and manual*, *Journal of High Energy Physics* **2006** (2006) 026, ISSN: 1029-8479, URL: <http://dx.doi.org/10.1088/1126-6708/2006/05/026>.
 - [30] T. Sjöstrand et al., *An introduction to PYTHIA 8.2*, *Computer Physics Communications* **191** (2015) 159, ISSN: 0010-4655, URL: <http://dx.doi.org/10.1016/j.cpc.2015.01.024>.
 - [31] G. Aad et al., *Observation of the associated production of a top quark and a Z boson in pp collisions at $\sqrt{s}=13$ TeV with the ATLAS detector*, *Journal of High Energy Physics* **2020** (2020), ISSN: 1029-8479, URL: [http://dx.doi.org/10.1007/JHEP07\(2020\)124](http://dx.doi.org/10.1007/JHEP07(2020)124).
 - [32] A. twiki, “ATLAS Isolation and Fake Forum”, 2021, URL: <https://twiki.cern.ch/twiki/bin/view/AtlasProtected/IsolationFakeForum>.
 - [33] G. Cowan et al., *Asymptotic formulae for likelihood-based tests of new physics*, *The European Physical Journal C* **71** (2011), ISSN: 1434-6052, URL: <http://dx.doi.org/10.1140/epjc/s10052-011-1554-0>.
 - [34] M. Pinamonti and et al., “TRExFitter”, URL: <https://trexfitter-docs.web.cern.ch/trexfitter-docs/>.
 - [35] W. Verkerke and D. Kirkby, *The RooFit toolkit for data modeling*, 2003, arXiv: [physics/0306116 \[physics.data-an\]](https://arxiv.org/abs/physics/0306116).
 - [36] L. Moneta et al., *The RooStats Project*, 2011, arXiv: [1009.1003 \[physics.data-an\]](https://arxiv.org/abs/1009.1003).
 - [37] *Luminosity determination in pp collisions at $\sqrt{s} = 13$ TeV using the ATLAS detector at the LHC*, tech. rep., CERN, 2019, URL: <https://cds.cern.ch/record/2677054>.
 - [38] G. Avoni et al., *The new LUCID-2 detector for luminosity measurement and monitoring in ATLAS*, *JINST* **13** (2018) P07017.
 - [39] Z. Marshall, *Simulation of Pile-up in the ATLAS Experiment*, *J. Phys. Conf. Ser.* **513** (2014) 022024, ed. by D. L. Groep and D. Bonacorsi.
 - [40] A. Salvucci, *Measurement of muon momentum resolution of the ATLAS detector*, *EPJ Web of Conferences* **28** (2012) 12039, ISSN: 2100-014X, URL: <http://dx.doi.org/10.1051/epjconf/20122812039>.
 - [41] M. Aaboud et al., *Electron efficiency measurements with the ATLAS detector using 2012 LHC proton–proton collision data*, *The European Physical Journal C* **77** (2017), ISSN: 1434-6052, URL: <http://dx.doi.org/10.1140/epjc/s10052-017-4756-2>.
 - [42] G. Aad et al., *Performance of pile-up mitigation techniques for jets in pp collisions at $\sqrt{s} = 8$ TeV using the ATLAS detector*, *Eur. Phys. J. C* **76** (2016) 581, arXiv: [1510.03823 \[hep-ex\]](https://arxiv.org/abs/1510.03823).
 - [43] *Expected performance of the ATLAS b-tagging algorithms in Run-2*, (2015), URL: <https://cds.cern.ch/record/2037697>.

Bibliography

- [44] M. Aaboud et al., *Measurement of the production cross-section of a single top quark in association with a Z boson in proton–proton collisions at 13 TeV with the ATLAS detector*, Physics Letters B **780** (2018) 557, ISSN: 0370-2693,
URL: <http://dx.doi.org/10.1016/j.physletb.2018.03.023>.
- [45] *Top Working Group Summary Plots–Autumn 2018*, tech. rep., CERN, 2018,
URL: <http://cds.cern.ch/record/2647993>.